

Bounds on the Uniaxial Effective Complex Permittivity of Two-phase Composites and Optimal or Near Optimal Microstructures

Kshiteej J. Deshmukh^{a,1,*}, Graeme W. Milton^a

^a*Department of Mathematics, University of Utah, Salt Lake City, 84101, UT, USA*

Abstract

Electromagnetic materials with a uniaxial effective permittivity tensor, characterized by its transverse (ϵ_{\perp}) and axial (ϵ_{\parallel}) components, play a central role in the design of advanced photonic and electromagnetic materials including hyperbolic metamaterials, and biological imaging platforms. Tight bounds on the complex effective permittivity of such metamaterials are critical for predicting and optimizing their macroscopic electromagnetic response. While rigorous tight bounds exist for isotropic two-phase composites, corresponding results for uniaxial composites remain relatively unexplored. In this work, we systematically investigate the attainable range of ϵ_{\perp} and ϵ_{\parallel} in the quasistatic regime for two-phase metamaterials with isotropic homogeneous phases. By analyzing known microgeometries and constructing hierarchical laminates (HLs), we demonstrate that the classical bounds on ϵ_{\perp} are not optimal. We conjecture improved bounds based on numerically fitted circular arcs derived from convex hulls of ϵ_{\perp} values obtained from HLs, and we identify optimal rank-4 HL structures that achieve all points on the conjectured bounds. Additionally, we quantify the correlation between ϵ_{\perp} and ϵ_{\parallel} for fixed volume fractions, and propose a design algorithm to construct HL microstructures achieving prescribed values of ϵ_{\perp} . Leveraging the Cherkasov-Gibiansky transformation and the translation method, we extend recent techniques developed for isotropic composites by Kern-Miller-Milton to derive translation bounds on the uniaxial complex effective permittivity tensor. Finally, bounds on the sensitivity of the effective permittivity tensor of low-loss composites are obtained and their optimality is shown in two-dimensions. Our results advance the theoretical understanding of uniaxial metamaterials and provide practical tools for the design of tailored anisotropic metamaterials.

Keywords: Homogenization, Two-phase composites, Hyperbolic metamaterials, Uniaxial complex effective permittivity,

1. Introduction

A material with a uniaxial permittivity tensor represented by the matrix ϵ is characterized by two of its eigenvalues in the directions orthogonal to the symmetry-axis being equal (transverse component denoted by

*Corresponding author

Email addresses: kdeshmukh@uh.edu (Kshiteej J. Deshmukh[✉]), graeme.milton@utah.edu (Graeme W. Milton[✉])

¹Now at, Department of Mechanical and Aerospace Engineering, University of Houston, Houston, 77204, TX, USA

ϵ_{\perp}), and the eigenvalue along the axis of symmetry is the axial component ϵ_{\parallel} , for instance,

$$\epsilon = \begin{bmatrix} \epsilon_{\perp} & 0 & 0 \\ 0 & \epsilon_{\perp} & 0 \\ 0 & 0 & \epsilon_{\parallel} \end{bmatrix}. \quad (1)$$

Uniaxial materials can be found in nature, e.g. calcite and quartz crystals, biological tissues like lipid bilayers, as well as can be artificially constructed, for example by taking a stack of sheets of two different isotropic dielectric materials. The study of effective uniaxial permittivity tensors of uniaxial dielectric composites has become increasingly important in electromagnetic applications. Recently, a computational microscopy method was used to determine the components of the uniaxial permittivity tensor and uncover the biological architecture of mouse brain tissue (Yeh et al., 2021, 2024). Hyperbolic metamaterials (Jacob et al., 2006; Salandrino and Engheta, 2006; Poddubny et al., 2013; Shekhar et al., 2014) (also known as HMMs) have gained a widespread interest due to their ability to resolve sub-wavelength objects as they can support propagation of large wavevectors. They are being used in several exotic applications like, optical negative refraction (Smith et al., 2004; Hoffman et al., 2007), spontaneous emission engineering (Noginov et al., 2010; Lu et al., 2014), and optical hyperlenses for sub-diffraction limit imaging (Jacob et al., 2006; Liu et al., 2007). HMMs represent a special class of dielectric metamaterials with uniaxial effective permittivity tensors where ideally ϵ_{\perp} and ϵ_{\parallel} are real and either $\epsilon_{\perp} < 0$ and $\epsilon_{\parallel} > 0$, or $\epsilon_{\perp} > 0$ and $\epsilon_{\parallel} < 0$. In practice, while one can have real positive modulus, the other modulus is complex with a negative real part and a small imaginary part. In this work, we focus on the more general quasistatic two-phase metamaterials with complex uniaxial effective permittivity tensors.

The study of effective permittivity in composite materials is a fundamental problem in electromagnetism, with significant implications for the design of dielectric materials, metamaterials, and photonic structures. Determining accurate bounds on the complex permittivity of such composites is essential for characterizing their macroscopic electromagnetic response. In this context, Schulgasser and Hashin (1976) analyzed a statistically homogeneous and isotropic two-phase composite where the constituent phases were low-loss dielectrics. Under the assumption that the imaginary part of the permittivity of each phase is small compared to the real part, they derived bounds on the effective complex permittivity of the composite. For isotropic two-phase composites with unknown or known volume fractions bounds on complex effective permittivity are given by the well-known Bergman-Milton (Milton, 1980; Bergman, 1980a; Milton, 1981a,b) bounds, which correspond to circular arcs in the complex plane. Recently, Kern et al. (2020) improved one of the circular arcs bounding the complex isotropic permittivity and showed that it is optimal, as it is attained by assemblages of doubly coated cylinders. Bounds on the transverse and axial components of the uniaxial complex effective permittivity for a two-phase composite were given by Milton (1981a), but the existence of optimal microstructures was not fully investigated, and the question of whether tighter bounds are possible remains unanswered.

In this work, we investigate the bounds and optimal microstructures pertaining to the problem of uniaxial effective permittivity of two-phase composites with isotropic homogeneous constituent phases in the quasistatic regime, i.e. under the assumption that the composite microscale variations occur at much smaller length

scales than the wavelength of the fields. The isotropic permittivity of the pure phases is denoted by ϵ_1 and ϵ_2 , and their respective volume fractions are f_1 and $1 - f_1$. The complex effective permittivity tensor is denoted by ϵ_* . Section 2 provides a brief background on the Bergman-Milton bounds. In Sections 2 and 3, we investigate the range of ϵ_\perp obtained by considering well-known simple geometries and hierarchical laminates (HLs). The results show that one of the bounds for the uniaxial case given by Milton (1981a) is likely not optimal. By numerically fitting circles to the convex hull of ϵ_\perp values obtained from Schulgasser laminates of hierarchical laminates we conjecture optimal bounds given by the fitted circular arcs. Tree structures of the HLs attaining points on the conjectured bounds are identified and they are rank-4 HLs. Laminates formed in more than one lamination step are called hierarchical laminates and the minimum number of sufficiently separated length scales in the subsequent lamination steps is defined as the rank of the hierarchical laminate.

From the perspective of designing uniaxial metamaterials it is highly desirable to know if ϵ_\perp or ϵ_\parallel , or both can be customized. Towards this end, in Section 4 we give the correlation between the axial and the transverse components of a given two-phase composite with fixed volume fraction. We also propose an algorithm to design a microstructure (specifically, a HL geometry) that achieves the exact specified value of ϵ_\perp if it lies in the interior of the region enclosed by the bounds.

Using the Cherkav-Gibiansky transformation (Cherkaev and Gibiansky, 1994) and the translation method (Tartar, 1985a; Murat and Tartar, 1985; Lurie and Cherkaev, 1982, 1984; Milton, 2002), Kern et al. (2020) proposed optimal bounds for the complex isotropic effective permittivity. Following their analysis we use the same translation tensor to find bounds for uniaxial complex effective permittivity. The corresponding results are given in Section 5. In Section 6, we obtain bounds on the sensitivity of the anisotropic effective permittivity in low-loss composites in two-dimensions.

All numerical calculations are performed using Python. The values of ϵ_1 , ϵ_2 , f_1 for all the plots in the paper are chosen to clearly illustrate the findings. Below is a list of common notations that will be used throughout this paper.

Notation

1. Electric displacement field - $d(x)$
2. Electric field - $e(x)$
3. Complex permittivity tensor - $\epsilon(x)$
4. Complex effective permittivity tensor- ϵ_*
5. Permittivity of phase-1 and phase-2 - ϵ_1 , ϵ_2 , respectively.
6. Volume fractions of phase-1 and phase-2 - f_1 and f_2 , respectively.
7. Transverse component of ϵ_* and axial component of ϵ_* - ϵ_\perp and ϵ_\parallel , respectively
8. Microgeometries are denoted as:
 - CC1 – Coated cylinder with phase 1 as core
 - CC2 – Coated cylinder with phase 2 as core
 - CE1 – Coated ellipsoid with phase 1 as core
 - CE2 – Coated ellipsoid with phase 2 as core
 - CEC1 – Coated elliptical cylinder with phase 1 as core

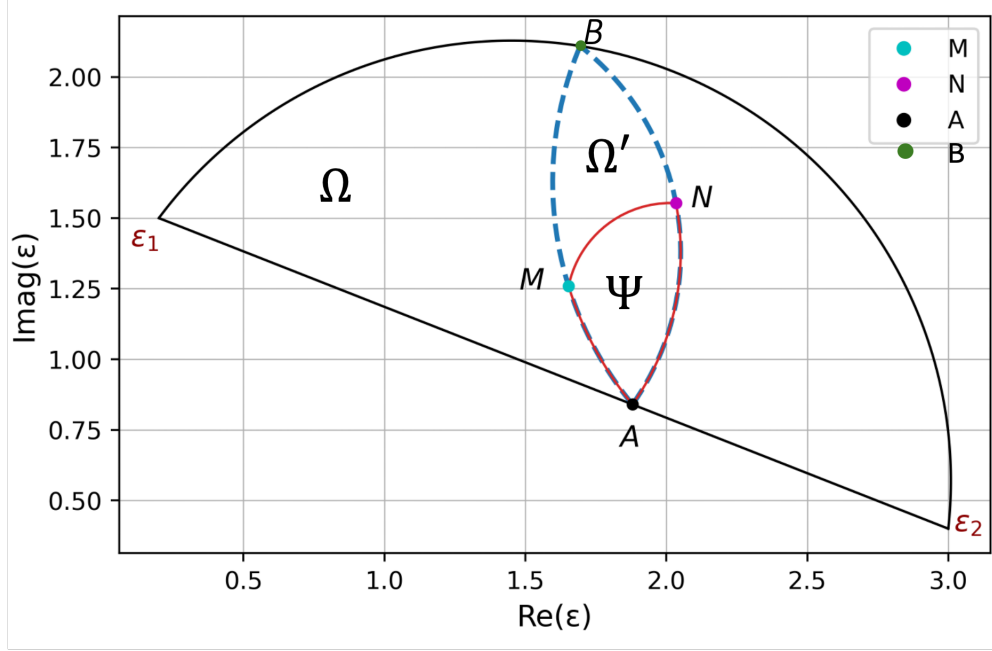


Figure 1: Bounds on the complex effective permittivity of a two-component composite with $\epsilon_1 = 0.2 + 1.5i$, $\epsilon_2 = 3 + 0.4i$, and $f_1 = 0.4$. The region Ω gives bounds on the effective permittivity when the volume fraction is unknown. Bounds on the transverse component ϵ_{\perp} of the uniaxial permittivity are shown by the solid red curves enclosing the region Ψ . The region Ψ is bounded by three circular arcs AM , MN , and AN . The axial component can lie anywhere in the region Ω' (shown by the dashed blue curve) bounded by the circular arcs AMB and ANB .

- CEC2 – Coated elliptical cylinder with phase 2 as core
- COS1 – Coated oblate spheroid with phase 1 as core
- COS2 – Coated oblate spheroid with phase 2 as core
- CPS1 – Coated prolate spheroid with phase 1 as core
- CPS2 – Coated prolate spheroid with phase 2 as core
- DCC1 – Doubly coated cylinder with phase 1 as core
- DCC2 – Doubly coated cylinder with phase 2 as core
- HS1 – Hashin-Shtrikman coated sphere assemblage with phase 1 as core
- HS2 – Hashin-Shtrikman coated sphere assemblage with phase 2 as core
- L – Simple laminates
- HL – Hierarchical laminates

2. Range of ϵ_{\perp} for a Two-phase Composite with Arbitrary Volume Fraction

Around 1980s, Bergman and Milton ([Bergman, 1980a](#); [Milton, 1980, 1981a,b](#)) derived bounds on the complex effective permittivity of a two-phase composite in the quasistatic limit. Depending on the known information of the composite these bounds were shown to be regions in the complex plane bounded by circular arcs. For a two-phase composite with isotropic and homogeneous component complex permittivities given by ϵ_1 and ϵ_2 , these bounds are summarized in Figure 1 as follows. If only the phase permittivities (ϵ_1, ϵ_2) are known then the effective permittivity ϵ_* , taken to be any diagonal element of the complex effective permittivity matrix ϵ_* ,

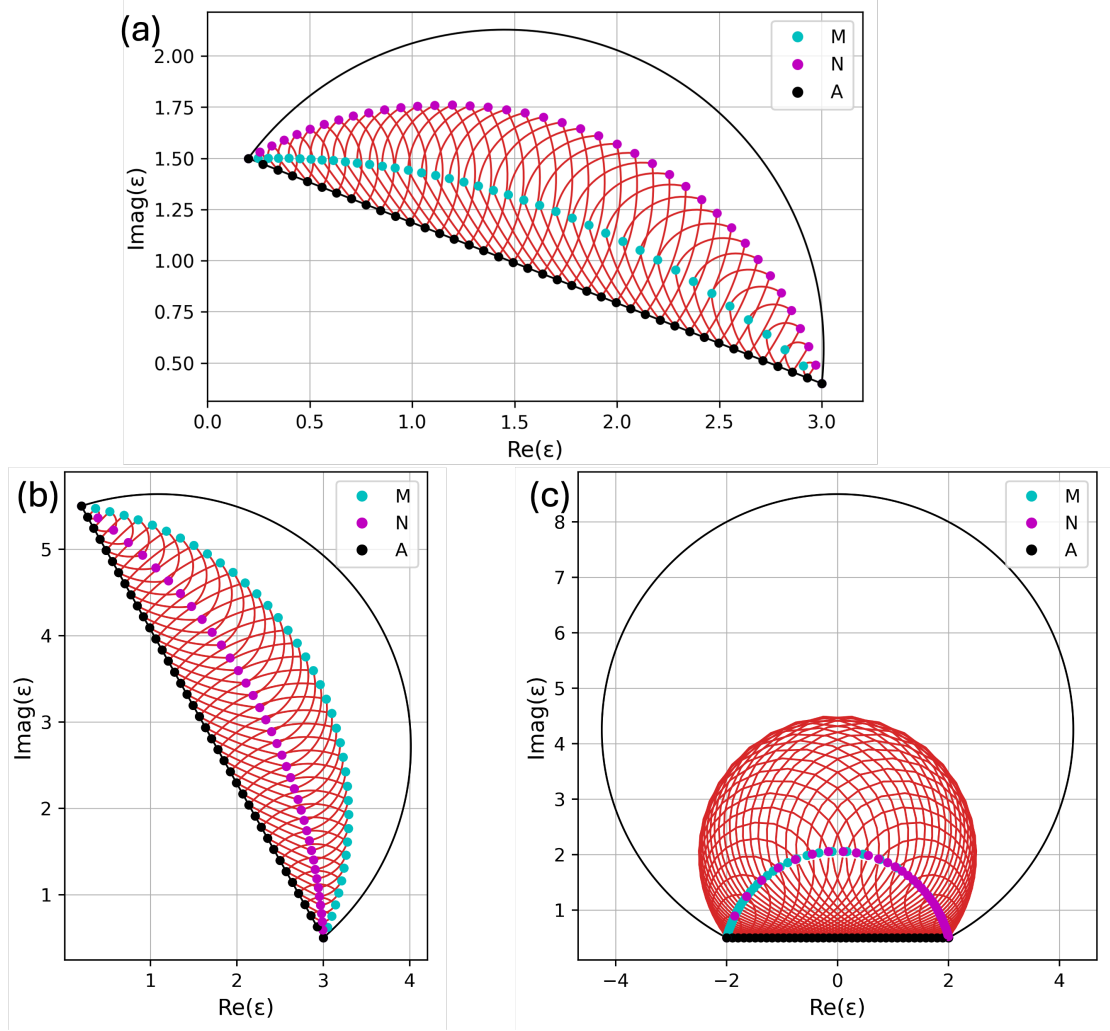


Figure 2: Bounds obtained from the union of Ψ regions by varying the volume fraction f_1 . Different values for ϵ_1 and ϵ_2 result in different parts of the region Ψ forming the bound. (a) $\epsilon_1 = 0.2 + 1.5i$, $\epsilon_2 = 3 + 0.4i$: Loci of N forms the bound. (b) $\epsilon_1 = 0.2 + 5.5i$, $\epsilon_2 = 3 + 0.5i$: Loci of M forms the bound. (c) $\epsilon_1 = -2 + 0.5i$, $\epsilon_2 = 2 + 0.5i$: Points on the boundary MN form the bound. Points N , M , and A are shown in pink, cyan, and black, respectively.

is restricted to the region Ω bounded between a straight line joining ϵ_1 and ϵ_2 , and a circular arc passing through ϵ_1 , ϵ_2 and the origin. If the volume fractions f_1 and $1 - f_1$ of the two phases are known, then ϵ_* is bounded by the lens shaped region Ω' (shown by dashed blue curves in Figure 1) bounded by two circular arcs AMB and ANB . The circular arc AMB is generated by the circle passing through the points A , B , ϵ_2 , and the arc ANB is generated by the circle passing through points A , B , ϵ_1 . For uniaxial composite materials, the effective permittivity has two of the three eigenvalues equal to each other, which we refer to as the transverse component of ϵ_* , and the remaining eigenvalue is the axial component. The axial component, $\epsilon_{||}$, can take any value in the region Ω' , but the transverse component, ϵ_{\perp} , is restricted to the region Ψ contained within Ω' and bounded by circular arcs AM , MN , and AN (colored in red in Figure 1). Since the focus of this paper is on effective complex uniaxial permittivities, we will not discuss the further bounds obtained in the isotropic case. In this section, we are interested in determining all the possible values attained by the

transverse component ϵ_{\perp} , i.e., the range of ϵ_{\perp} , for a composite material with known phase permittivities but arbitrary volume fractions of the phases. A simple way to do that is to look at the bounds formed by the union of the regions Ψ as the volume fraction f_1 is varied from 0 to 1 for given values of (ϵ_1, ϵ_2) . Figure 2 shows the range of ϵ_{\perp} generated by plotting the Ψ regions as the volume fraction f_1 is varied. Depending on the phase permittivities of the composite, the outer bound may be formed by the loci of points N (purple), loci of points M (cyan), or by points on the arc MN (red curves) as seen in Figures 2(a)-(c), respectively. The other part of boundary of the union of the Ψ regions in each case is formed by the loci of points A (black).

3. Effective Uniaxial Permittivities From Known Microgeometries

When dealing with bounds on effective properties, it is natural and extremely desirable to find the optimal microgeometries. While the bounds on uniaxial permittivity by Milton (1981a) (discussed above) were given more than four decades ago, the uniaxial microgeometries that fill up the region Ψ have not been explored. Using the Schulgasser lamination technique (Schulgasser, 1977a), one can construct uniaxial effective permittivity tensors from composites with diagonal permittivity tensors. For such a material, the permittivity can be represented by $\epsilon = \text{Diag}[\lambda_1, \lambda_2, \lambda_3]$, where λ_i ($i = 1, 2, 3$) denote the principal permittivities. Previously, Schulgasser laminates were constructed to obtain hierarchical laminates with an isotropic effective permittivity given by $\text{tr}(\epsilon_*)/3$ from an anisotropic material (Schulgasser, 1977a; Kern et al., 2020). Here, we use a similar Schulgasser lamination scheme, but stop after a single lamination step (such a scheme was used in Milton (1981a)). Suppose we construct a composite by laminating this anisotropic material with volume fraction f along the direction \mathbf{n} parallel to the x_1 -axis (principal direction corresponding to λ_1) with a 90° rotation of itself about the x_1 -axis with permittivity tensor $\epsilon_0 = \text{Diag}[\lambda_1, \lambda_3, \lambda_2]$ and volume fraction $1 - f$. Then the effective permittivity of this laminate is simply given by taking the arithmetic and harmonic means as,

$$\epsilon_* = \begin{bmatrix} \lambda_1 & 0 & 0 \\ 0 & f\lambda_2 + (1-f)\lambda_3 & 0 \\ 0 & 0 & f\lambda_3 + (1-f)\lambda_2 \end{bmatrix} \quad (2)$$

When $f = 0.5$, we get the uniaxial permittivity tensor $\epsilon_* = \text{Diag}[\lambda_1, (\lambda_2 + \lambda_3)/2, (\lambda_3 + \lambda_2)/2]$. Hereafter in this article, we consider laminates with only orthogonal directions of lamination, and we refer to the uniaxial laminates created by this scheme in (2) as the Schulgasser laminates. For a given anisotropic tensor ϵ with $\lambda_1 \neq \lambda_2 \neq \lambda_3$, one can generate three different uniaxial laminates by constructing Schulgasser laminates along each of the three principal directions. This implies that for a given anisotropic tensor $\epsilon = \text{Diag}[\lambda_1, \lambda_2, \lambda_3]$, we can construct three uniaxial laminates with the transverse components given by $(\lambda_2 + \lambda_3)/2$, $(\lambda_1 + \lambda_3)/2$, $(\lambda_1 + \lambda_2)/2$, and their respective axial components as $\lambda_1, \lambda_2, \lambda_3$.

We first investigate the range of ϵ_{\perp} of the Schulgasser laminates constructed from well-known microgeometries, and then identify the optimal microstructures and also those that fill the region Ψ . The effective permittivity ϵ_* of an assemblage of confocal coated ellipsoids (CE) with a core of phase 1 can be obtained

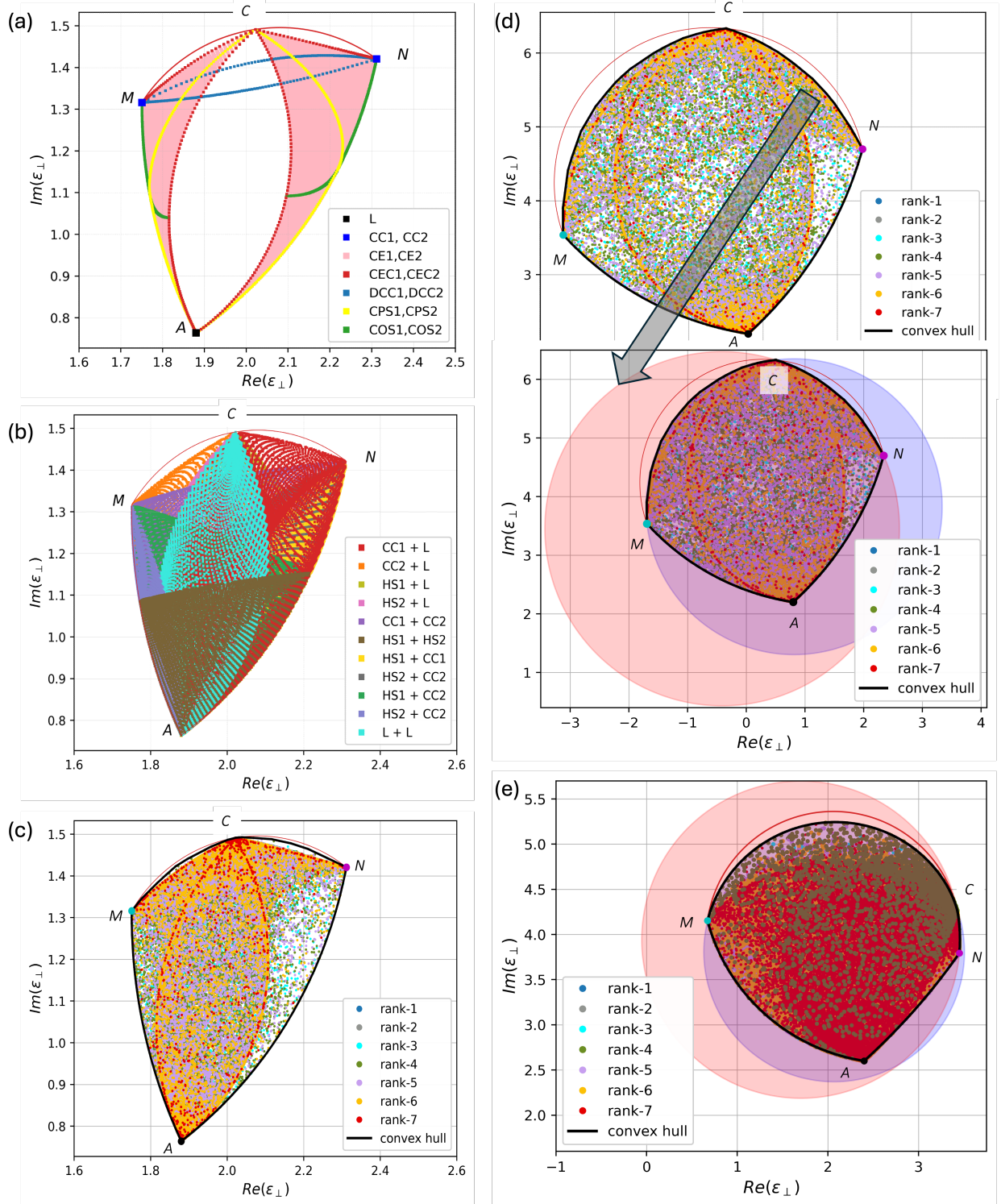


Figure 3: Microgeometries filling the region Ψ and conjectured optimal bounds. (a)-(c) show results for a composite with $\epsilon_1 = 0.2 + 1.76i$, $\epsilon_2 = 3 + 0.1i$, and $f_1 = 0.4$. The ranges of ϵ_{\perp} (shown by colored markers) are obtained from Schulgasser laminates of: (a) assemblages of well-known microgeometries where points A, M, and N are attained by the L, CC1, and CC2 geometries respectively, (b) assemblages of mixed microgeometries, (c) HL geometries. The convex hull of range of ϵ_{\perp} is shown by the solid black curve. (d)-(e) show results for a composite with $\epsilon_1 = -4 + 1i$, $\epsilon_2 = 4 + 3i$, and $f_1 = 0.4$. and $f_1 = 0.2$, respectively. The red circle is fitted to the points on the boundary CN of the convex hull (the grey arrow in (d) points to the red circle that is fitted to points on the boundary CN), and similarly the blue circle is fitted to points on the boundary MC of the convex hull.

from the relation (Milton, 1981a, 2002; Tartar, 1985b):

$$f_1 \epsilon_2 (\epsilon_* - \epsilon_2 \mathbf{I})^{-1} = \epsilon_2 (\epsilon_1 - \epsilon_2)^{-1} \mathbf{I} + f_2 \mathbf{M}, \quad (3)$$

where \mathbf{M} is related to the depolarization tensors \mathbf{D}_c and \mathbf{D}_e of the core and the exterior elliptical surfaces respectively, by the relation $\mathbf{M} = (\mathbf{D}_c - f_1 \mathbf{D}_e)/f_2$. It was shown that $\text{tr } \mathbf{M} = 1$, and that \mathbf{M} is positive semi-definite. As the shape of the coated ellipsoids is varied keeping the volume fraction f_1 fixed, \mathbf{M} varies over all positive semi-definite symmetric matrices satisfying $\text{tr } \mathbf{M} = 1$. As the coated ellipsoids are confocal the depolarization tensors \mathbf{D}_c and \mathbf{D}_e are not independent of each other. If the principal axes of the ellipsoids are chosen as the coordinate system, then \mathbf{M} , \mathbf{D}_c , \mathbf{D}_e are diagonal matrices. Special cases of the coated ellipsoid geometry can be obtained depending on the depolarization factors. For coated spheroids, the tensor $\mathbf{M} = \text{Diag}[1 - 2m, m, m]$ with $m \in [0, 1/2]$ as two of the depolarization factors are equal. They can be further distinguished into coated prolate and coated oblate spheroids with the same tensor $\mathbf{M} = \text{Diag}[1 - 2m, m, m]$ but with $m \in [0, 1/3]$ and $m \in [1/3, 1/2]$, respectively. For coated elliptical cylinders (CEC), one of the depolarization factors is 0 and we get the tensor $\mathbf{M} = \text{Diag}[m, 1 - m, 0]$ with $m \in [0, 1]$.

Figure 3(a) shows the range of ϵ_\perp obtained from the Schulgasser laminates of assemblages of CEs and assemblages of doubly coated cylinders (DCC). The parts of the boundary AM and AN are attained using coated oblate and prolate spheroids (shown in green and yellow, respectively) as noted in Bergman (1980b). The boundary of Ω' is also attained by coated elliptical cylinders as noted in Milton (1981a). Schulgasser laminates of assemblages of CEC (shown in red) achieve only points M , N , and C on the boundary MCN . At the point C , the CEC geometry degenerates to a simple laminate geometry. Among the already uniaxial geometries, point A is attained by simple laminate (L) geometry, whereas the points M and N are obtained from assemblages of coated cylinders with phase-1 as core (CC1) and phase-2 as core (CC2) respectively. The transverse component for an assemblage of CC1 geometry is given by the relation (Hashin, 1962; Hashin and Shtrikman, 1962),

$$\epsilon_\perp = \epsilon_2 + \frac{2f_1 \epsilon_2 (\epsilon_1 - \epsilon_2)}{2\epsilon_2 + f_2 (\epsilon_1 - \epsilon_2)}. \quad (4)$$

The transverse component of assemblages of the DCC1 geometry with the core and outermost cylinders of phase-1 with volume fractions p_1 and p_3 and the middle cylindrical shell of phase-2 with volume fraction $p_2 = 1 - p_1 - p_3$ can be given as (Schulgasser, 1977b),

$$\epsilon_\perp = \epsilon_1 + \frac{2(p_1 + p_2)\epsilon_1}{p_3 - \frac{2\epsilon_1}{\epsilon_1 - \epsilon_0}}, \quad (5)$$

where

$$\epsilon_0 = \epsilon_2 + \frac{2p_1/(1 - p_3)\epsilon_2}{p_2/p_3 - 2\frac{\epsilon_2}{\epsilon_2 - \epsilon_1}}. \quad (6)$$

Analogous expressions hold for the DCC2 geometry with a core of phase 2. By varying the volume fractions p_1 and p_3 of the core and outer cylinders (phase-1) while keeping the volume fraction $p_2 = 1 - f_1$ (phase-2) fixed, we get the blue curve in Figure 3(a) showing the range of transverse components of DCC1 and DCC2

assemblages.

Laminate geometries can be constructed from assemblages of different geometries; for instance, assuming sufficient separation of scales, an assemblage of CC can be laminated with an assemblage of coated spheres to get an effective permittivity tensor (which maybe anisotropic), and further Schulgasser laminates of these structures can be constructed to obtain uniaxial laminates. Figure 3(b) shows the range of ϵ_{\perp} of Schulgasser laminates of such mixed geometries. Schulgasser laminates of a simple laminate (L) with a 90° rotation of itself yields the point C on the boundary MN of the region Ψ with the transverse component given by,

$$\epsilon_{\perp} = \frac{1}{2} \left(f_1 \epsilon_1 + f_2 \epsilon_2 + \frac{1}{f_1/\epsilon_1 + f_2/\epsilon_2} \right). \quad (7)$$

Both Figures 3(a)-(b) show that the bounds AM and AN are optimal as those can be attained by coated oblate and prolate spheroids, and mixtures of coated cylinder and laminate geometries. However, only three points on the arc MCN have been attained.

3.A. Conjectured Bounds on the Transverse Component of the Uniaxial Permittivity

The laminates constructed by laminating two phases in more than one step (assuming sufficient separation of scales at every subsequent step) are called hierarchical laminates (HL). The minimum number of length scales required for their construction is typically referred to as the rank of the hierarchical laminate. The simple laminate geometry L is a rank-1 laminate structure formed by laminating two pure phases in one step. For a rank-2 laminate, the rank-1 laminate (core phase) is further laminated with one of the pure phases or another rank-1 laminate (coating phase). In subsequent lamination steps, the laminate generated in the previous step is laminated with one of the pure phases or any one of the previously generated laminates, thereby generating higher ranked laminates. In this paper, we consider HLs where subsequent lamination directions are orthogonal to each other, and hence there are only three possible lamination directions, i.e. along the x_1 , x_2 , and x_3 axes. Finally, to obtain uniaxial geometries we consider Schulgasser laminates of the HL, thereby adding a lamination step and increasing the rank by one of the given HL. The other geometries can be seen as special cases of the HL geometries since CC1 and CC2 can be replaced by HL (as can all the geometries listed in 8 of the notation section).

For given ϵ_1, ϵ_2 values of the pure phase with a fixed volume fraction f_1 , we numerically construct about a million HLs ranging from rank-1 to rank-8. The range of ϵ_{\perp} of the Schulgasser laminates of these HLs is shown in Figure 3(c). It is observed that HLs can densely populate the region Ψ and attain points everywhere, except close to the arc MCN . A convex hull of all the ϵ_{\perp} values obtained from the HLs is plotted and shown by the solid black curve in Figure 3. The convex hull shows that optimal HL microstructures can attain all points on the black arcs AN and AM , while the only points attained on the boundary MCN in this case too are M , C , and N . This observation is common to other composites considered in the analysis, for example, in Figure 3(d)-(e) we consider a composite with $\epsilon_1 = -4 + 1i$, $\epsilon_2 = 4 + 3i$, and $f_1 = 0.4$ (the values are arbitrarily chosen to clearly show the plots), and one can observe from the convex hull that only points M , C , and N are attained on the boundary. This suggests that the original bound corresponding to arc MCN (shown by solid red curve) is not the best possible, and that tighter bounds may exist.

On further analysis of the convex hulls considered for several examples in our analysis, we find that the

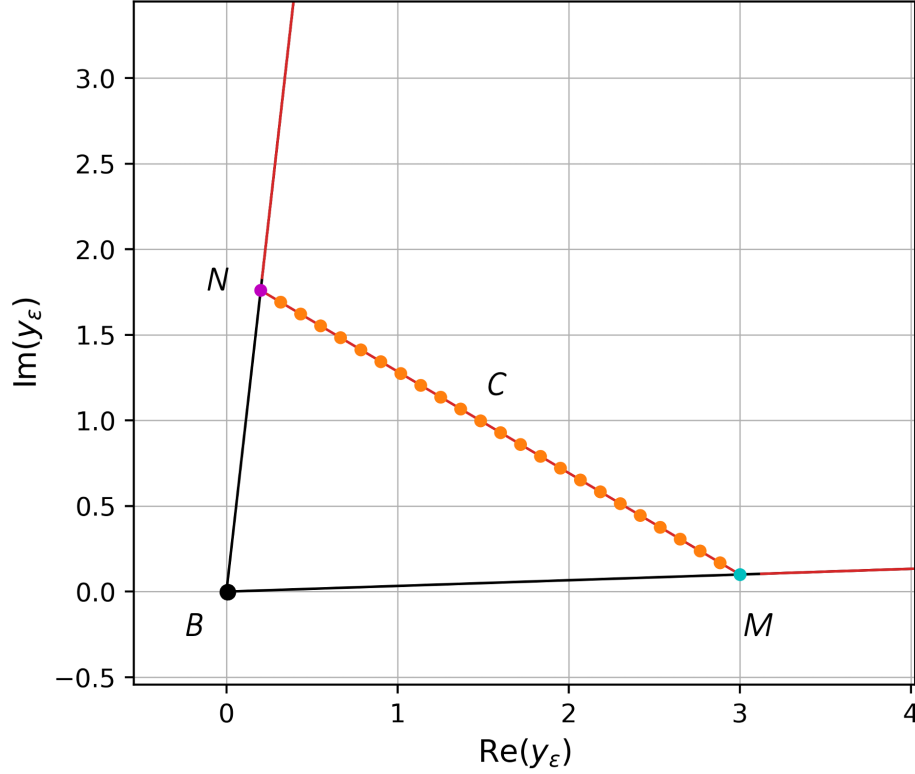


Figure 4: Y-transform of the region Ψ (bounded by the red straight lines extending from points M and N to infinity, and the line segment MN) is shown with points M , N , B , and C shown in cyan, pink, black, and orange, respectively, for composite with $\epsilon_1 = 0.2 + 1.76i$, $\epsilon_2 = 3 + 0.1i$. In the y -plane, the region Ψ is volume fraction independent and the point C , attained by the Schulgasser laminate of L , traces the bound given by the straight line joining points M and N (which corresponds to the circular arc MCN in the bounds given by Milton (1981a)).

parts of the boundary MC and NC of the convex hull that we label Γ can be fit to a good accuracy by two circular arcs; one passing through the points M and C , and the other passing through the points N and C , respectively. In Figure 3(d) the red shaded circle fits the boundary NC of $\partial\Gamma$ and the blue shaded circle fits the boundary MC of $\partial\Gamma$. Hence, we propose that the fitted circular arcs MC and NC on Γ are the conjectured optimal bounds on ϵ_\perp obtained numerically. In our numerical calculations, we observe that the fitted red and blue circles corresponding to the conjectured bounds do not pass through any obvious third point (even in the Y-transformed plane - see Milton (2002) for definition) that can completely characterize the circles. We will refer to the fitted circular arcs MC and NC on Γ , as the blue circular arc MC and the red circular arc NC , respectively. Figure 3(e) shows the conjectured bounds given by the blue circular arc MC and red circular arc NC on $\partial\Gamma$ for the same composite with $\epsilon_1 = -4 + 1i$, $\epsilon_2 = 4 + 3i$, but $f_1 = 0.2$. These numerical results show that the original region Ψ which was bounded by three circular arcs, is now bounded by four circular arcs.

Following work of Christian Kern (private communication) it is interesting to see what the bounds look in the y_ϵ plane, where $y_\epsilon(\epsilon_*) = -f_2\epsilon_1 - f_1\epsilon_2 + f_1f_2(\epsilon_1 - \epsilon_2)(f_1\epsilon_1 + f_2\epsilon_2 - \epsilon_*)^{-1}(\epsilon_1 - \epsilon_2)$, is the Y-transform of ϵ_* . The reason for this is that bounds often simplify when plotted in this plane, and are often volume fraction independent when plotted in this plane. The region Ψ is indeed simpler in the y_ϵ plane and forms a truncated

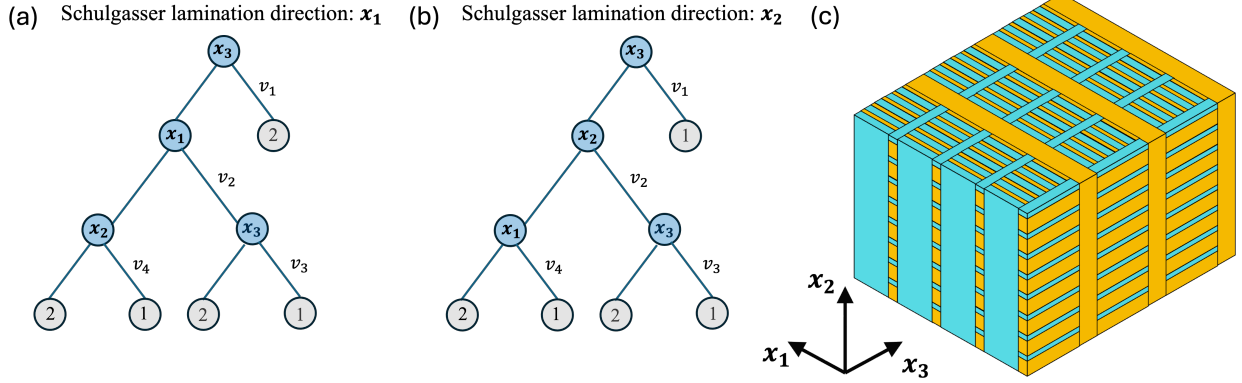


Figure 5: Tree structures of the rank-3 hierarchical laminate (HL) attaining all points on the conjectured bounds when a subsequent Schulgasser lamination step is made. (a) Tree structure of rank-3 HL attaining points on the conjectured bound given by blue circular arc MC of $\partial\Gamma$. The numbers inside the grey nodes denote the pure phase, and the blue nodes contain the lamination direction at every step. The general volume fractions of the laminating phases associated with the tree edges are denoted by v_1, v_2, v_3 , and v_4 . (b) Tree structure of the rank-3 HL attaining points on the conjectured bound given by red circular arc NC of $\partial\Gamma$. (c) The microgeometry of the rank-3 HL laminate represented by the tree structure in (a) is shown with phase-1 in blue and phase-2 in yellow. Schulgasser lamination in the x_1 direction with a 90° rotation of itself about the x_1 axis gives the optimal rank-4 HL.

wedge shaped region bounded by the red straight lines and the line segment MN (Figure 4). Two sides of this region are attained by the coated ellipsoid geometries, while the point C (after the Y-transformation) traces the third line segment MN as the volume fraction is varied. Thus, the Y-transformation of the conjectured bounds are volume fraction dependent, and thus, cannot be derived using any method that gives volume fraction independent bounds on y_ϵ (such as the standard analytic method or the standard translation method).

3.B. Hierarchical Laminates Corresponding to the Conjectured Bounds

The conjectured bounds are obtained by fitting circles to the ϵ_\perp values obtained from the Schulgasser laminates of HLs. We now focus on finding the specific structure of the hierarchical laminates that attain the points on the conjectured bounds. A useful way of describing hierarchical laminates is by representing the lamination sequence using a tree structure (Milton, 2002; Kern et al., 2020) (see Ch. 9 in Milton (2002)). Specifically, every hierarchical laminate can be represented as a tree structure in which each node has either zero or two children. The nodes with zero children, commonly known as leaves, correspond to one of the pure phases. Conversely, any node that is not a leaf represents a laminate formed from its child nodes and is associated with a particular lamination direction. For the three-dimensional HLs considered in this work with subsequent directions of lamination being orthogonal, there are only three possible lamination directions (along the x_1 , x_2 , and x_3 axes). In our representation of the tree structure, the numbers inside the leaf nodes correspond to the pure phase (phase-1 or phase-2), and every node that is not a leaf has the lamination direction written in it.

The ϵ_\perp values forming the convex hull and attaining the points on the conjectured bounds in Figures 3(d)-(e) were found to be obtained from rank-4 hierarchical laminates. Our goal then is to find a rank-4 tree family that realizes all the points on the conjectured bounds given by the blue circular arc MC on $\partial\Gamma$ and the red circular arc NC on $\partial\Gamma$. Figure 5(a) shows a rank-3 (that gives a rank-4 HL after forming a Schulgasser laminate along the x_1 direction) HL tree family where by appropriately varying the volume

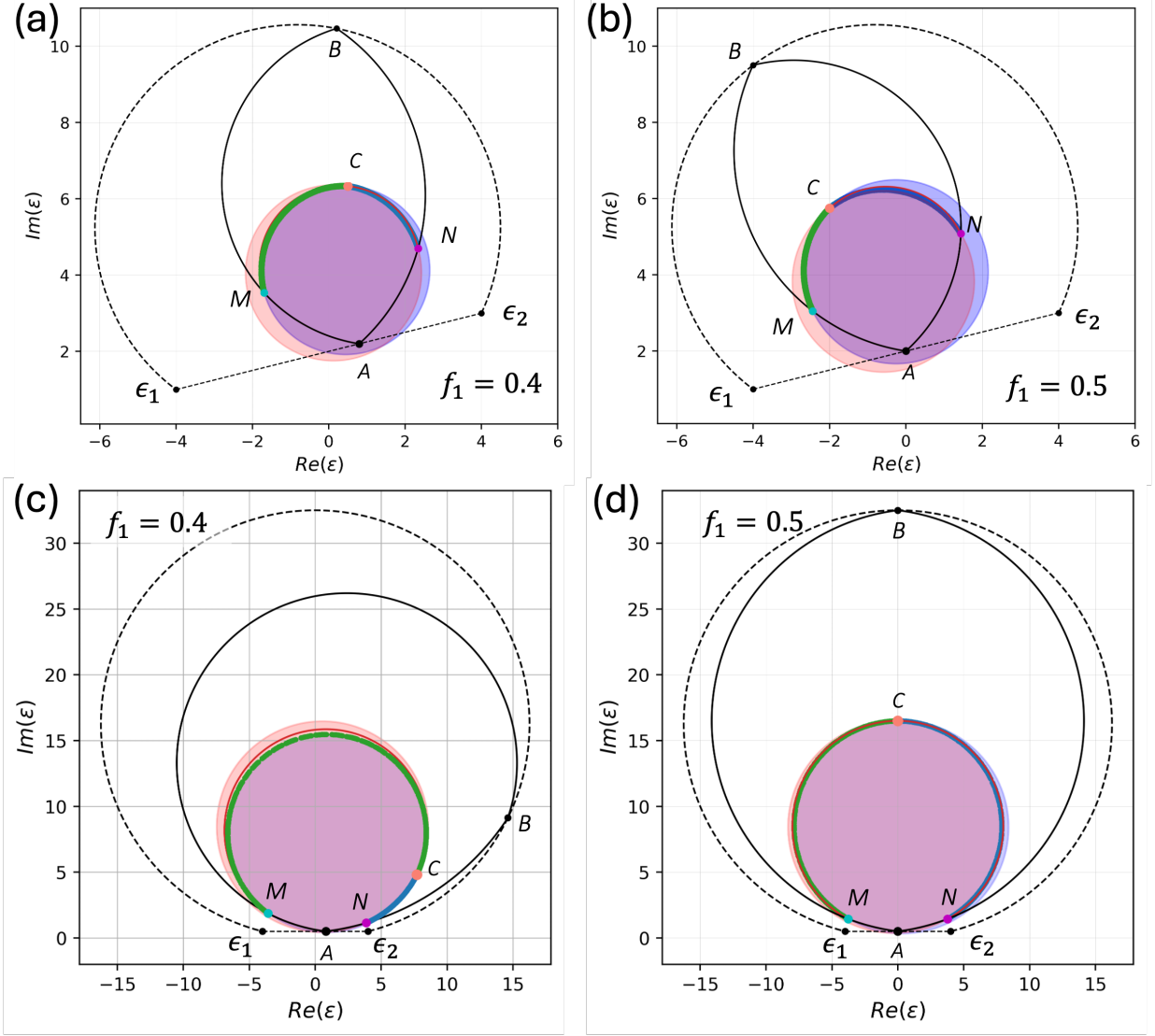


Figure 6: Range of ϵ_{\perp} obtained from optimal rank-4 hierarchical laminates attaining green points on the blue circular arc MC of $\partial\Gamma$ and blue points on the red circular arc NC of $\partial\Gamma$ of the conjectured bounds. The classical Bergman-Milton bound on ϵ_{\perp} is shown by the solid red curve. (a) $\epsilon_1 = -4 + 1i$, $\epsilon_2 = 4 + 3i$, and $f_1 = 0.4$. (b) $\epsilon_1 = -4 + 1i$, $\epsilon_2 = 4 + 3i$, and $f_1 = 0.5$. (c) $\epsilon_1 = -4 + 0.5i$, $\epsilon_2 = 4 + 0.5i$, and $f_1 = 0.4$. (d) $\epsilon_1 = -4 + 0.5i$, $\epsilon_2 = 4 + 0.5i$, and $f_1 = 0.5$.

fractions v_1, v_2, v_3, v_4 (which are as indicated in Figure 5) of the subsequent lamination steps while keeping f_1 fixed gives the blue circular arc MC of $\partial\Gamma$. The volume fraction f_1 for the rank-3 tree family in Figure 5(a) is given as,

$$f_1 = (v_4(1 - v_2) + v_3v_2)(1 - v_1) \quad (8)$$

Similarly, Figure 5(b) shows a rank-3 HL tree family that attains the points on the conjectured bound given by red circular arc NC of $\partial\Gamma$. The volume fraction f_1 for this rank-3 tree family can be obtained from the relation,

$$f_1 = (v_4(1 - v_2) + v_3v_2)(1 - v_1) + v_1 \quad (9)$$

Varying the volume fractions v_1, v_2, v_3, v_4 while keeping f_1 fixed, gives ϵ_\perp values in the interior as well, along with the points attained on the conjectured bounds. Interchanging phase-1 and phase-2 in the rank-3 HL tree structure of Figure 5(a) gives that of Figure 5(b), and vice-versa. The optimal HL microstructure corresponding to the rank-3 tree (which becomes rank-4 after the Schulgasser laminate construction) in Figure 5(a) is shown in Figure 5(c) with the phase-1 shown in blue and the phase-2 shown in yellow.

In Figure 6(a), the green points on the conjectured bound, blue circular arc MC of $\partial\Gamma$, are the ϵ_\perp values obtained from the family of rank-3 HL shown in Figure 5(a) by varying the volume fractions v_i while keeping $f_1 = 0.4$ fixed for a composite with $\epsilon_1 = -4 + 1i$, $\epsilon_2 = 4 + 3i$. Similarly, the blue points on the conjectured bound, red circular arc NC of $\partial\Gamma$, are the ϵ_\perp values obtained from the family of rank-3 HL shown in Figure 5(b). For the same composite at a different volume fraction $f_1 = 0.5$, the optimal ϵ_\perp values attaining points on the conjectured bounds are shown in Figure 6(b). Figures 6(c)-(d) show the results for a different composite, with $\epsilon_1 = -4 + 0.5i$, $\epsilon_2 = 4 + 0.5i$, and $f_1 = 0.4$ and $f_1 = 0.5$, respectively. In each case, the optimal ϵ_\perp values are attained using the same tree families shown in Figure 5. Our numerical simulations indicate that the axial components of the optimal HLs form two tiny loops of blue and green curves near the point A , but these could be artifacts of numerical computation.

4. Correlating the Transverse and Axial Components

In applications that require tailored uniaxial permittivity tensors, it is highly desirable to know for a given transverse component what are the correlated axial components, and vice-versa. In this section, we use HL geometries to explore the correlated axial components of a given fixed value of ϵ_\perp . A challenge here is to find HL geometries that exactly achieve the value of a given ϵ_\perp . Suppose for a two-phase composite with fixed volume fractions, we are interested in finding the range of correlated axial components for a given fixed transverse component denoted by ϵ_\perp^0 . We first estimate the feasible range of $\partial^2\epsilon_\perp/\partial\epsilon_1^2$ that is compatible with the given transverse component ϵ_\perp^0 , and then find the range of the correlated feasible region for the axial component.

For two-phase composites with principal permittivities given by $\lambda_1(\epsilon_1, \epsilon_2)$, $\lambda_2(\epsilon_1, \epsilon_2)$, and $\lambda_3(\epsilon_1, \epsilon_2)$, Bergman (1978) obtained the result

$$\sum_{i=1,2,3} \frac{\partial^2 \lambda_i(\epsilon_1, 1)}{\partial \epsilon_1^2} \Big|_{\epsilon_1=1} = -2f_1f_2. \quad (10)$$

For uniaxial laminates we have two of the principal permittivities equal to each other, so letting $\epsilon_{\parallel} = \lambda_1$, and $\epsilon_{\perp} = \lambda_2 = \lambda_3$ we get,

$$2 \frac{\partial^2 \epsilon_{\perp}}{\partial \epsilon_1^2} \Big|_{\epsilon_1=1} = -2f_1 f_2 - \frac{\partial^2 \epsilon_{\parallel}}{\partial \epsilon_1^2} \Big|_{\epsilon_1=1}. \quad (11)$$

Another constraint on the the second partial derivatives is given by the bounds derived by [Wiener \(1912\)](#),

$$\frac{\partial^2 \lambda_i(\epsilon_1, 1)}{\partial \epsilon_1^2} \Big|_{\epsilon_1=1} \leq 0, \quad (12)$$

for $i = 1, 2, 3$. Using (11) and (12) we get the result ([Milton, 1981a](#)),

$$0 \geq \frac{\partial^2 \epsilon_{\perp}}{\partial \epsilon_1^2} \Big|_{\epsilon_1=1} \geq -f_1 f_2 \quad (13)$$

Another corollary of (10) is that isotropic two-phase composites having isotropic permittivity ϵ_* , have the property

$$\frac{\partial^2 \epsilon_*(\epsilon_1, 1)}{\partial \epsilon_1^2} \Big|_{\epsilon_1=1} = -2f_1 f_2 / d, \quad (14)$$

where the d is the dimension ([Bergman, 1978](#)). [Bergman \(1980a\)](#) and [Milton \(1980\)](#) obtained bounds on the complex isotropic permittivity of a two-phase composite in the isotropic case, i.e., when information about the second partial derivative is known. These bounds can be written in terms of the second partial derivatives and give the well-known lens shaped bounds. One of the arcs of the lens is given by the curve traced by $\epsilon_+(u_1)$,

$$\epsilon_+(u_1) = f_1 \epsilon_1 + f_2 \epsilon_2 - \left(\frac{-1}{2} \frac{\partial^2 \epsilon_*}{\partial \epsilon_1^2} \Big|_{\epsilon_1=1} \right) \frac{(\epsilon_2 - \epsilon_1)^2}{(u_1 \epsilon_1 + u_2 \epsilon_2)} \quad (15)$$

as u_1 is varied so that, $1 + \frac{1}{2f_2} \frac{\partial^2 \epsilon_*}{\partial \epsilon_1^2} \Big|_{\epsilon_1=1} \geq u_1 \geq \frac{-1}{2f_2} \frac{\partial^2 \epsilon_*}{\partial \epsilon_1^2} \Big|_{\epsilon_1=1}$, and $u_1 + u_2 = 1$. The other arc that completes the bounds is given by $\epsilon_-(u_1)$,

$$\epsilon_-(u_1) = \left(f_1 / \epsilon_1 + f_2 / \epsilon_2 + \left(-f_1 f_2 - \frac{1}{2} \frac{\partial^2 \epsilon_*}{\partial \epsilon_1^2} \Big|_{\epsilon_1=1} \right) \frac{(1/\epsilon_2 - 1/\epsilon_1)^2}{(u_1/\epsilon_1 + u_2/\epsilon_2)} \right)^{-1}, \quad (16)$$

where u_1 is varied so that, $f_2 - \frac{1}{2f_2} \frac{\partial^2 \epsilon_*}{\partial \epsilon_1^2} \Big|_{\epsilon_1=1} \geq u_1 \geq f_2 + \frac{1}{2f_1} \frac{\partial^2 \epsilon_*}{\partial \epsilon_1^2} \Big|_{\epsilon_1=1}$, and $u_1 + u_2 = 1$.

4.A. Axial Components Correlated to a Given Transverse Component

The main idea now is to use the bounds in an inverse manner to bound the second derivative $\frac{\partial^2 \epsilon_*}{\partial \epsilon_1^2}$, when the transverse component ϵ_{\perp}^0 is given. For every value of $\frac{\partial^2 \epsilon_*}{\partial \epsilon_1^2} \Big|_{\epsilon_1=1}$, (15) and (16) give two arcs forming a lens shaped region within the region Ω' . For isotropic composites as stated in (14) we have a single fixed value of $\frac{\partial^2 \epsilon_*}{\partial \epsilon_1^2} \Big|_{\epsilon_1=1}$ which gives us through relations (15) and (16) a single lens shaped region, which has been well-described in previous works. For the transverse and axial components of a uniaxial composite, however,

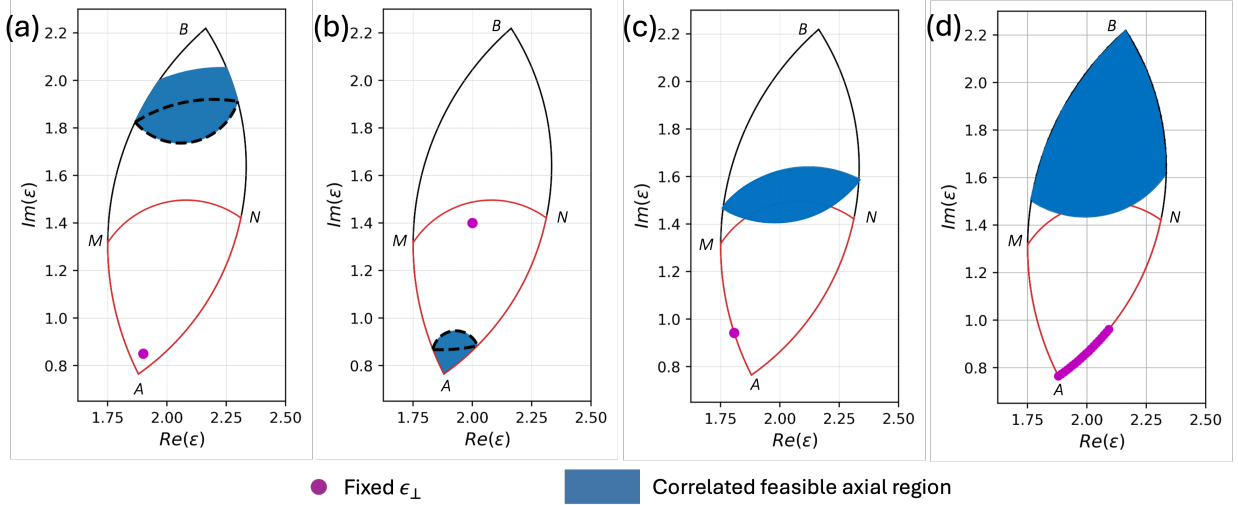


Figure 7: The correlated feasible regions for the axial components of a two phase composite with $\epsilon_1 = 0.2 + 1.76i$, $\epsilon_2 = 3 + 0.1i$, and $f_1 = 0.4$. The fixed transverse component ϵ_\perp^0 is shown by the purple marker. The feasible region for the range of correlated axial components is shown in blue. The blue regions are formed by the union of the lens shaped regions of the type shown by the dashed black curve. (a) For fixed $\epsilon_\perp^0 = 1.9 + 0.85i$ in the interior of the region Ψ . (b) For fixed $\epsilon_\perp^0 = 2 + 1.4i$ in the interior of the region Ψ . (c) For fixed ϵ_\perp^0 on the boundary AM . (d) For ϵ_\perp^0 forming part of the boundary AN .

there is a range of possible values that $\frac{\partial^2 \epsilon_\perp}{\partial \epsilon_1^2} \Big|_{\epsilon_1=1}$ and $\frac{\partial^2 \epsilon_\parallel}{\partial \epsilon_1^2} \Big|_{\epsilon_1=1}$ can take as described by the relations (11) and (13).

For a given fixed transverse component ϵ_\perp^0 , we vary $\frac{\partial^2 \epsilon_\perp}{\partial \epsilon_1^2} \Big|_{\epsilon_1=1}$ within the limits given by (13) and select only those values of $\frac{\partial^2 \epsilon_\perp}{\partial \epsilon_1^2}$ such that the associated lens shaped regions contain the point ϵ_\perp^0 . Using (11), we can find the $\frac{\partial^2 \epsilon_\parallel}{\partial \epsilon_1^2} \Big|_{\epsilon_1=1}$ value corresponding to each $\frac{\partial^2 \epsilon_\perp}{\partial \epsilon_1^2} \Big|_{\epsilon_1=1}$ value that is compatible with ϵ_\perp^0 . For these second partial derivatives of the axial component we again plot the lens shaped regions and take their union to get the feasible region for the correlated axial component.

For a composite with $\epsilon_1 = 0.2 + 1.76i$, $\epsilon_2 = 3 + 0.1i$, and $f_1 = 0.4$, Figure 7(a) shows the given transverse component ϵ_\perp^0 (shown by the purple marker) in the interior of the region Ψ . The correlated axial feasible region is shown by the blue region which is formed by the union of the lens shaped regions compatible with the range of values of $\frac{\partial^2 \epsilon_\parallel}{\partial \epsilon_1^2}$. Figure 7(b) shows the correlated feasible regions of the transverse and axial components for a different point in the interior. In Figure 7(c), for a point on the boundary AM of the region Ψ , we get only one value of $\frac{\partial^2 \epsilon_\perp}{\partial \epsilon_1^2}$ compatible with the point ϵ_\perp^0 (purple marker) and the correlated axial feasible region is also given by a single lens shaped region (in blue). The correlated feasible regions for a part of the boundary AN are shown in Figure 7(d).

For a given fixed transverse component ϵ_\perp^0 , our goal now is to find HL geometries that achieve exactly the transverse component ϵ_\perp^0 and then find the corresponding axial components for each of these HL geometries. We develop a triangulation algorithm to realize HL geometries that give exactly the desired value ϵ_\perp^0 of the

transverse component provided that ϵ_{\perp}^0 lies in the interior of the region Ψ . The main idea of the algorithm is briefly stated in 1. This construction method ensures that the new HL formed is also axially symmetric.

Algorithm 1 Triangulation algorithm to generate HL microstructures with a specified value of the transverse component ϵ_{\perp}^0

1. First generate a large number of HL geometries so that the range of ϵ_{\perp} values sufficiently populates the region Ψ .
2. Randomly choose three points from the range of generated ϵ_{\perp} points to form a triangle and determine if ϵ_{\perp}^0 lies inside the triangle.
3. ϵ_{\perp}^0 lies inside the triangle if its barycentric coordinates lie within the range $[0, 1]$ and if their sum is less than 1.
4. If the point is in the interior, then a higher rank HL is constructed by laminating the HLs (which are uniaxial) corresponding to the vertices of the triangle with the lamination direction such that all the three HLs have their axes of symmetry along the lamination direction.
5. The volume fractions for the HLs are chosen as the barycentric coordinates of the point ϵ_{\perp}^0 .

However, this scheme will not work if ϵ_{\perp}^0 lies on the boundary of the region Ψ .

Figure 8(a) shows the range of correlated axial components (shown by orange markers) for a given transverse component (shown by the purple marker) obtained from HL geometries. Note that these points lie within the blue region described in the previous section and illustrated in Figure 7. Figure 8(b) shows the correlated axial components for a different transverse point in the interior of the region Ψ . For ϵ_{\perp}^0 on the boundary, HL geometries with the exact fixed transverse component may be very difficult to find. In this case, we generate a large number of HL geometries and rely on obtaining values of the transverse component within a ball of certain radius centered at ϵ_{\perp}^0 . The radius of the ball is suitably chosen to achieve desired numerical

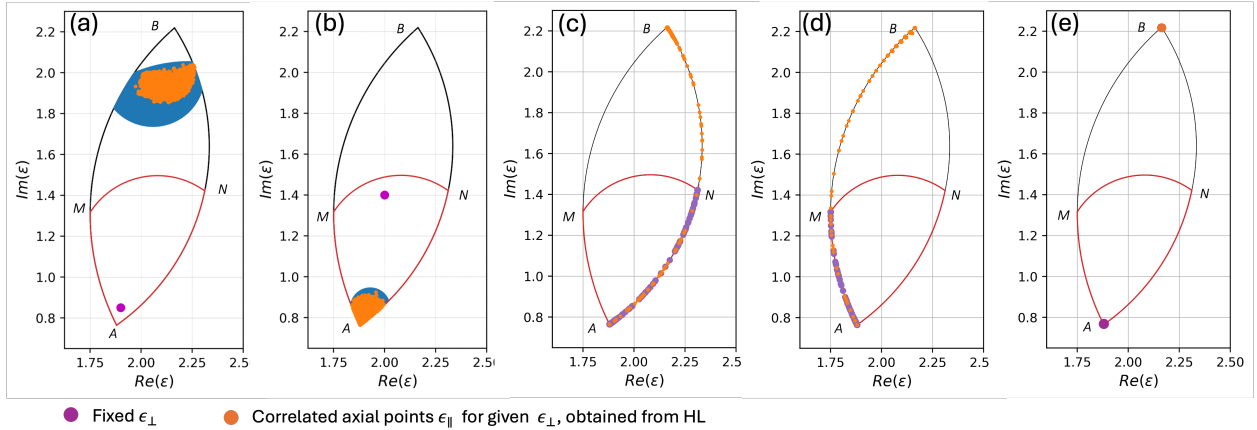


Figure 8: The correlated axial components of the given fixed transverse components obtained from the Schulgasser laminates of HL geometries for a composite with $\epsilon_1 = 0.2 + 1.76i$, $\epsilon_2 = 3 + 0.1i$, and $f_1 = 0.4$. (a)-(b) The axial feasible regions are shown in blue color. The fixed transverse component is shown by the purple marker, which is taken to be $\epsilon_{\perp}^0 = 1.9 + 0.85i$ for (a), and $\epsilon_{\perp}^0 = 2 + 1.4i$ for (b). The range of the axial components of the Schulgasser laminates of HL geometries correlated with the fixed transverse component is shown by the orange markers. (c)-(d) For fixed ϵ_{\perp}^0 (purple markers) on the boundaries AN and AM , the correlated axial components ϵ_{\parallel} (orange markers) lie on the boundary ANB and AMB , respectively. (e) For $\epsilon_{\perp}^0 = 1.9 + 0.85i$ equal to the point A , the correlated axial component ϵ_{\parallel} is found to be the point B .

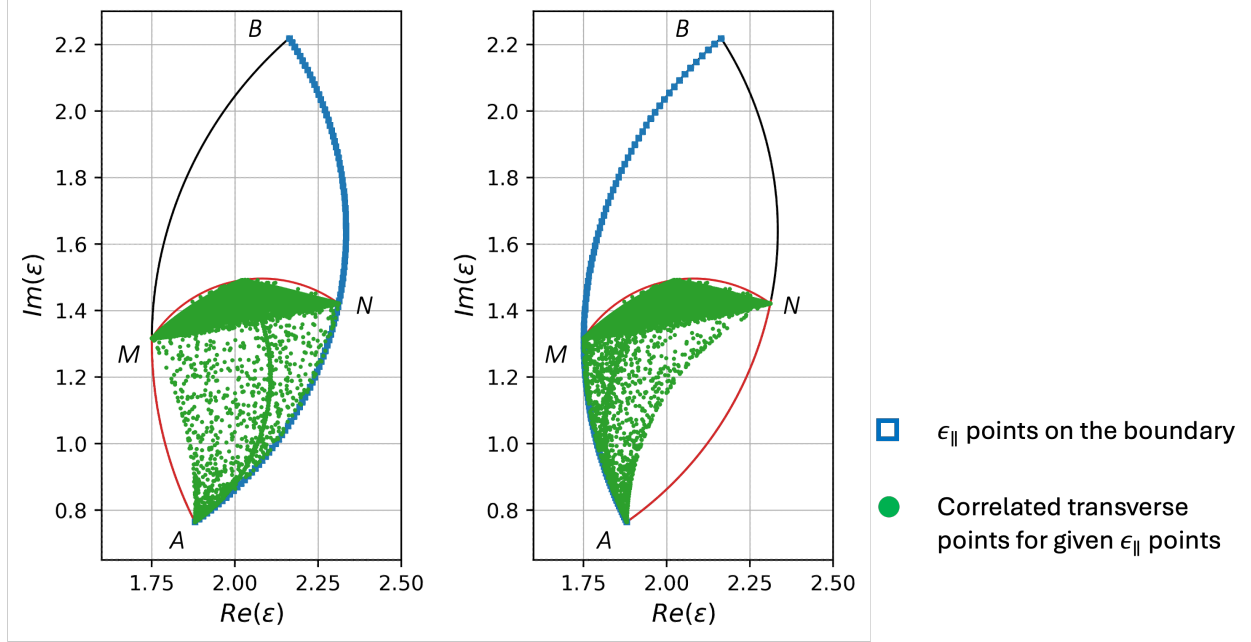


Figure 9: The correlated transverse components of the given fixed axial components obtained from HL geometries for a composite with $\epsilon_1 = 0.2 + 1.76i$, $\epsilon_2 = 3 + 0.1i$, and $f_1 = 0.4$. (a)-(b) For fixed $\epsilon_{||}^0$ (blue markers) on the boundaries ANB and AMB , the correlated transverse components (green markers) lie on the boundary AN and boundary AM , respectively, as well as in the interior of the region Ψ .

accuracy and ideally should tend to 0. Figure 8(c) shows that for ϵ_{\perp}^0 points (purple markers) along the boundary AN , the correlated axial points (orange markers) are observed to lie along the arc ANB . Similarly, Figure 8(d) shows that the correlated axial components of the transverse components on the boundary MN , lie on the arc AMB . Finally in Figure 8(e), we observe that the only correlated axial component of the transverse component given by point A is the point B .

One can perform a similar analysis to obtain correlated transverse components for a given fixed axial component denoted by $\epsilon_{||}^0$. Here, we consider just two cases of fixed axial components on the boundaries AMB and ANB . We observe from Figures 9(a)-(b) that the correlated transverse components of the given fixed axial components (shown in blue) on the boundary ANB (AMB), lie on the boundary AN (AM) as well as in the interior of the region Ψ .

5. Bounds on the Complex Uniaxial Permittivity Using the Method of Translations

Our analysis so far suggests that, the bounds of Milton (1981a) on the complex uniaxial effective permittivity of two-phase composites are not optimal, specifically the bound given by the boundary MN of the region Ψ shown in Figure 1. Using the Cherkaev and Gibiansky (1994) transformation and the method of translations (Tartar, 2018; Lurie and Cherkaev, 1984; Murat and Tartar, 1985), Kern et al. (2020) derived an optimal bound on the complex isotropic effective permittivity of two-phase composites. Following a similar procedure we derive bounds on the complex effective permittivity of a uniaxial two-phase composite. The constitutive relations relating the electric field $e(x)$ and the electric displacement $d(x)$ are rewritten in terms of the real

parts (primed) and the imaginary parts (double primed) of the field quantities as,

$$\begin{bmatrix} \mathbf{e}'' \\ \mathbf{d}'' \end{bmatrix} = \begin{bmatrix} (\epsilon'')^{-1} & (\epsilon'')^{-1}\epsilon' \\ \epsilon'(\epsilon'')^{-1} & \epsilon'(\epsilon'')^{-1}\epsilon' + \epsilon'' \end{bmatrix} \begin{bmatrix} -\mathbf{d}' \\ \mathbf{e}' \end{bmatrix} = \mathbf{L} \begin{bmatrix} -\mathbf{d}' \\ \mathbf{e}' \end{bmatrix}, \quad (17)$$

where \mathbf{L} is a symmetric and positive definite second-order tensor. The corresponding minimization principle (Cherkaev and Gibiansky, 1994) to find the effective permittivity tensor can be stated as

$$\begin{bmatrix} -\mathbf{d}'_0 \\ \mathbf{e}'_0 \end{bmatrix} \cdot \mathbf{L}_* \begin{bmatrix} -\mathbf{d}'_0 \\ \mathbf{e}'_0 \end{bmatrix} = \min \left\{ \left\langle \begin{bmatrix} -\mathbf{d}' \\ \mathbf{e}' \end{bmatrix} \cdot \mathbf{L} \begin{bmatrix} -\mathbf{d}' \\ \mathbf{e}' \end{bmatrix} \right\rangle \mid \begin{array}{l} \langle \mathbf{d}' \rangle = \mathbf{d}'_0, \quad \nabla \cdot \mathbf{d}' = 0 \\ \langle \mathbf{e}' \rangle = \mathbf{e}'_0, \quad \nabla \times \mathbf{e}' = 0 \end{array} \right\}, \quad (18)$$

where $\langle \cdot \rangle$ denotes a volume average. Following the arguments and methods used in Kern et al. (2020), the problem in (18) is embedded in a problem involving a fourth-order tensor \mathcal{L} comprising several copies of \mathbf{L} . Let \mathcal{E} denote the fourth-order tensor given in the component form by

$$\mathcal{E}_{ijkl} = \epsilon_{ik}\delta_{jl}, \quad i, j, k, l = 1, 2, 3, \quad (19)$$

then the tensor \mathcal{L} is given in terms of \mathcal{E} as,

$$\mathcal{L} = \begin{bmatrix} (\mathcal{E}'')^{-1} & (\mathcal{E}'')^{-1}\mathcal{E}' \\ \mathcal{E}'(\mathcal{E}'')^{-1} & \mathcal{E}'(\mathcal{E}'')^{-1}\mathcal{E}' + \mathcal{E}'' \end{bmatrix}. \quad (20)$$

It is convenient to introduce the Y-transform (see Ch. 19 in Milton (2002) and references therein) of the effective tensor \mathcal{E}_* given by the relation,

$$\mathcal{Y} = -f_1\mathcal{E}_2 - f_2\mathcal{E}_1 + f_1f_2(\mathcal{E}_1 - \mathcal{E}_2) \cdot (f_1\mathcal{E}_1 + f_2\mathcal{E}_2 - \mathcal{E}_*)^{-1}(\mathcal{E}_1 - \mathcal{E}_2), \quad (21)$$

using which we can write the Y-transform of the effective tensor \mathcal{L}_* as,

$$\mathbf{Y} = \begin{bmatrix} (\mathcal{Y}'')^{-1} & -(\mathcal{Y}'')^{-1}\mathcal{Y}' \\ -\mathcal{Y}'(\mathcal{Y}'')^{-1} & \mathcal{Y}'(\mathcal{Y}'')^{-1}\mathcal{Y}' + \mathcal{Y}'' \end{bmatrix}. \quad (22)$$

We omit a detailed discussion of the procedure, which is discussed in sufficient detail in Kern et al. (2020), and instead directly use the important results. Using the Y-transform \mathbf{Y} we get the simple bounds,

$$\mathbf{Y} + \mathbf{T} \geq 0, \quad (23)$$

where the translation tensor \mathbf{T} is chosen such that \mathbf{T} is quasiconvex (Murat and Tartar, 1985; Lurie and Cherkaev, 1984; Tartar, 1985a; Gibiansky and Milton, 1993) and the translated tensors $\mathcal{L}_1 - \mathbf{T} \geq 0$ and $\mathcal{L}_2 - \mathbf{T} \geq 0$ are positive semi definite. We choose the same form for \mathbf{T} as the one used in Kern et al. (2020) that is

$$\mathbf{T} = \begin{bmatrix} \mathbf{A}(-t_1, 2t_1, 0) & \mathbf{A}(-t_3, -t_3, -t_3) \\ \mathbf{A}(-t_3, -t_3, -t_3) & \mathbf{A}(-2t_2, t_2, -t_2) \end{bmatrix} \quad (24)$$

where $t_1 \geq 0$, t_2, t_3 are arbitrary, and \mathbf{A} is a general fourth-order isotropic tensor given in the component form by

$$A_{ijkl}(t_1, t_2, t_3) = \frac{t_1}{3} \delta_{ij} \delta_{kl} + \frac{t_2}{2} \left(\delta_{ik} \delta_{jl} + \delta_{il} \delta_{jk} - \frac{2}{3} \delta_{ij} \delta_{kl} \right) + \frac{t_3}{2} (\delta_{ik} \delta_{jl} - \delta_{il} \delta_{jk}). \quad (25)$$

The effective uniaxial permittivity ϵ_* can be decomposed as linear combination of two orthogonal tensors

$$\epsilon_* = \epsilon_{\perp} (\mathbf{I} - \mathbf{n} \otimes \mathbf{n}) + \epsilon_{\parallel} \mathbf{n} \otimes \mathbf{n}, \quad (26)$$

using which we can write the fourth-order tensor \mathcal{E}_* from (19) in the component form as

$$\mathcal{E}_{*ijkl} = \epsilon_{\perp} (\delta_{ik} - n_i n_k) \delta_{jl} + \epsilon_{\parallel} n_i n_k \delta_{jl}. \quad (27)$$

Here, \mathbf{n} is the direction parallel to the axis of symmetry of the uniaxial composite. Substituting the above in (21) the Y-transform of the above fourth-order tensor is given by

$$\mathcal{Y}_{ijkl} = A_1 A_{ijkl}(1, 1, 1) + A_2 n_i n_k \delta_{jl} = A_1 (\delta_{ik} - n_i n_k) \delta_{jl} + (A_2 + A_1) n_i n_k \delta_{jl}, \quad (28)$$

where,

$$\begin{aligned} A_1 &= -f_1 \epsilon_2 - f_2 \epsilon_1 + \frac{f_1 f_2 (\epsilon_1 - \epsilon_2)^2}{f_1 \epsilon_1 + f_2 \epsilon_2 - \epsilon_{\perp}}, \\ A_2 &= -f_1 f_2 (\epsilon_1 - \epsilon_2)^2 \left(\frac{1}{f_1 \epsilon_1 + f_2 \epsilon_2 - \epsilon_{\perp}} - \frac{1}{f_1 \epsilon_1 + f_2 \epsilon_2 - \epsilon_{\parallel}} \right). \end{aligned} \quad (29)$$

The second equality in (28) is convenient for getting the inverse of \mathcal{Y} . It also implies that A_1 is the Y-transformed transverse component and $(A_1 + A_2)$ is the Y-transformed axial component.

Next, substitute (28) in (22), and together with the chosen form of the translation \mathbf{T} , substitute the result in the translation bounds given in (23). The positive semi definiteness constraint $\mathbf{Y} + \mathbf{T} \geq 0$ can be simplified to positive semi definiteness conditions on smaller submatrices by identifying the coupling terms. These conditions are:

$$\begin{bmatrix} t_1 + \frac{1}{(A_1 + A_2)''} & -\sqrt{2}t_1 & -t_3 - \frac{(A_1 + A_2)'}{(A_1 + A_2)''} & 0 \\ -\sqrt{2}t_1 & \frac{1}{A_1''} & 0 & -t_3 - \frac{A_1'}{A_1''} \\ -t_3 - \frac{(A_1 + A_2)'}{(A_1 + A_2)''} & 0 & (A_1 + A_2)'' + \frac{(A_1 + A_2)'^2}{(A_1 + A_2)''} & -\sqrt{2}t_2 \\ 0 & -t_3 - \frac{A_1'}{A_1''} & -\sqrt{2}t_2 & -t_2 + A_1'' + \frac{A_1'^2}{A_1''} \end{bmatrix} \geq 0, \quad (30)$$

$$\begin{bmatrix} 2t_1 + \frac{1}{A_1''} & -t_3 - \frac{A_1'}{A_1''} \\ -t_3 - \frac{A_1'}{A_1''} & t_2 + A_1'' + \frac{A_1'^2}{A_1''} \end{bmatrix} \geq 0, \quad (31)$$

and

$$\begin{bmatrix} \frac{1}{A_1''} & 0 & -t_3 - \frac{A_1'}{A_1''} & 0 \\ 0 & \frac{1}{A_1''} & 0 & -t_3 - \frac{A_1'}{A_1''} \\ -t_3 - \frac{A_1'}{A_1''} & 0 & \frac{|A_1|^2}{A_1''} & -t_3 \\ 0 & -t_3 - \frac{A_1'}{A_1''} & -t_3 & \frac{|A_1|^2}{A_1''} \end{bmatrix} \geq 0. \quad (32)$$

These conditions cannot be further simplified, and they imply that the determinants of the two 4×4 matrices and the one 2×2 matrix are non-negative. The translation parameters t_1, t_2, t_3 are chosen so that the translated tensors $\mathcal{L}_i - \mathbf{T}$ are positive semi definite, which implies the following two necessary and sufficient non-negativity conditions on the translation parameters (Kern et al., 2020)

$$(y'_c + \epsilon'_i)^2 + (y''_c + \epsilon''_i)^2 \geq R^2, \quad (33)$$

and

$$(y'_c - 2\epsilon'_i)^2 + (y''_c - 2\epsilon''_i)^2 \leq R^2, \quad (34)$$

where

$$y'_c = -\frac{t_3}{t_1}, \quad y''_c = -\frac{1 + 2t_1t_2 - t_3^2}{2t_1}, \quad \text{and } R = \left| \frac{1 - 2t_1t_2 + t_3^2}{2t_1} \right|. \quad (35)$$

These restrictions correspond to choice of t_1, t_2, t_3 such that $2\epsilon_1$ and $2\epsilon_2$ do not lie outside of the circle and $-\epsilon_1$ and $-\epsilon_2$ do not lie inside of the circle. The extremal translation parameters consistent with the restrictions correspond to the halfspace bounded by a straight line between $2\epsilon_1$ and $2\epsilon_2$ that does not contain $-\epsilon_1$ and $-\epsilon_2$, and one of the two circles passing through $2\epsilon_1, 2\epsilon_2$, and $-\epsilon_1$ or $-\epsilon_2$. This extremal choice of translations was obtained in Kern et al. (2020), and is directly used for our case since we are using exactly the same translation tensor.

We observe through numerically testing the constraints (30)-(32), that the particular choice of the isotropic translation tensor considered in this work does not give tighter bounds on ϵ_\perp when ϵ_\parallel is unknown or on ϵ_\parallel when ϵ_\perp is unknown, and that in fact these bounds are poorer than the original bounds given by Milton (1981a). However, they do give bounds correlating ϵ_\perp and ϵ_\parallel . The fact that our translation bound does not improve the bounds on ϵ_\perp and ϵ_\parallel is to be expected. Clearly the bounds on ϵ_\perp are optimal in the Y-transformed plane. The improved bound in Kern et al. (2020) in the isotropic case is on the side nearest A , so similarly one expects in this case it would be if $\frac{\partial^2 \epsilon_\perp}{\partial \epsilon_1^2} \Big|_{\epsilon_1=1} = -f_1 f_2$.

In the limit $\epsilon_\perp \rightarrow \epsilon_\parallel$, we have $A_2 \rightarrow 0$, and when $\epsilon_\perp = \epsilon_\parallel$ we get the isotropic case. The bounds given by (30)-(32) in this case reduce to the tight bounds on the effective isotropic permittivity given by Kern et al. (2020). Now assume that the uniaxial permittivity tensor is a perturbation of the isotropic permittivity tensor such that $\epsilon_\parallel = \alpha \epsilon_\perp$, i.e, the transverse component differs from the axial component by a small amount when the scalar α is close to 1. For the case when $\alpha = 1.1$, we numerically evaluate the translation bounds on ϵ_\perp , which we expect to be a perturbation of the isotropic tight bounds given by Kern et al. (2020). The numerical bounds on ϵ_\perp obtained from the constraints (30)-(32), with the assumption that the transverse and

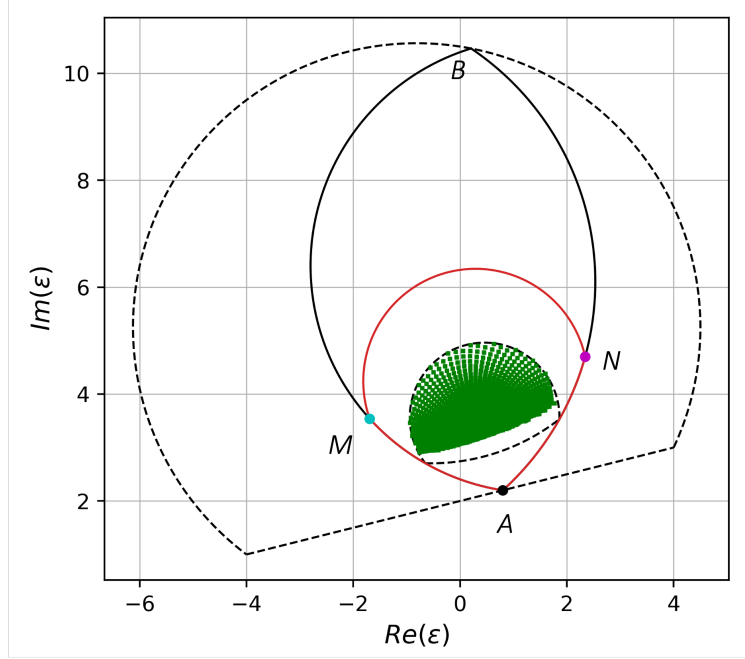


Figure 10: Numerically evaluated translation bounds on ϵ_{\perp} shown by the area shaded in green when ϵ_{\perp} and ϵ_{\parallel} are correlated as $\epsilon_{\parallel} = 1.1\epsilon_{\perp}$ for a composite with $\epsilon_1 = -4 + 1i$, $\epsilon_2 = 4 + 3i$, and $f_1 = 0.4$. When $\epsilon_{\perp} = \epsilon_{\parallel}$, it corresponds to the case of isotropic effective permittivity, and we recover the translation bounds obtained by [Kern et al. \(2020\)](#) and are shown by the dashed black curves. The green region lies within the region enclosed by the dashed black curves. (b) Y-transform of the region Ψ (bounded by the red straight lines and the line passing through points M and N) is shown with points M , N , B , and C shown in cyan, pink, black, and orange, respectively, for composite with $\epsilon_1 = 0.2 + 1.76i$, $\epsilon_2 = 3 + 0.1i$ and unknown volume fraction. In the Y-plane, the region Ψ is volume fraction independent, and the point C attained by the L geometry traces the bound given by the straight line joining points M and N (which corresponds to the circular arc MCN in the bounds given by [Milton \(1981a\)](#)). This shows that Ψ is optimal when the volume fractions are not fixed.

axial components have the correlation $\epsilon_{\parallel} = 1.1\epsilon_{\perp}$, are shown in Figure 10 by the green region. The lens shaped region given by the dashed black curve are the tight isotropic bounds (when $\epsilon_{\perp} = \epsilon_{\parallel}$ or $\alpha = 1$) given by [Kern et al. \(2020\)](#). As $\alpha \rightarrow 1$ the green region extends to fill up the region bounded by the black dashed curves. Thus, the translation bounds given here in (30)-(32) are useful at least when ϵ_{\perp} and ϵ_{\parallel} differ only by a small fixed amount.

6. Bounds on the Sensitivity of the Complex Effective Permittivity

In this section, our goal is to find bounds on the sensitivity of the anisotropic effective permittivity with respect to the phase permittivity in low-loss composites. We will show that in two-dimensions, bounds on the sensitivity lead to optimal bounds on the effective permittivity in the low-loss limit. [Schulgasser and Hashin \(1976\)](#) obtained bounds on the effective permittivity of low-loss composites by using bounds on $\partial\epsilon_{*}/\partial\epsilon_i$ ($i = 1, 2$) given by [Prager \(1969\)](#) for the case of statistically homogeneous isotropic two-phase composites with no loss.

6.A. Known Bounds

Let the Y-transform $\mathbf{Y}(\epsilon_*)$ of the effective permittivity be given by

$$\mathbf{Y}(\epsilon_*) = -f_2\epsilon_1 - f_1\epsilon_2 + f_1f_2(\epsilon_1 - \epsilon_2)(f_1\epsilon_1 + f_2\epsilon_2 - \epsilon_*)^{-1}(\epsilon_1 - \epsilon_2) \quad (36)$$

From the analytic properties of the function $\epsilon_*(\epsilon_1, \epsilon_2)$ it follows that $\mathbf{Y}_*(\epsilon_1, \epsilon_2)$ satisfies

1. The Herglotz property

$$\text{Im} [\mathbf{Y}_*(\epsilon_1, \epsilon_2)] \geq 0, \quad (37)$$

when both $\text{Im}(\epsilon_1) > 0, \text{Im}(\epsilon_2) > 0$.

2. The homogeneity property

$$\mathbf{Y}_*(\lambda\epsilon_1, \lambda\epsilon_2) = \lambda\mathbf{Y}_*(\epsilon_1, \epsilon_2). \quad (38)$$

Without loss of generality, by relabeling the phases if necessary, we may assume $\text{Im}[\epsilon_1/\epsilon_2] > 0$. Letting λ appropriately approach $1/\epsilon_2$ we get

$$\text{Im} [\mathbf{Y}_*(\epsilon_1/\epsilon_2, 1)] = \text{Im} [\mathbf{Y}_*(\epsilon_1, / \epsilon_2)/\epsilon_2] \geq 0. \quad (39)$$

Similarly, letting λ appropriately approach $-1/\epsilon_1$ we get

$$\text{Im} [\mathbf{Y}_*(\epsilon_1, / \epsilon_2)/\epsilon_1] \leq 0. \quad (40)$$

Equations (39) and (40) are the wedge bounds written in an equivalent form in Milton (1987) formulae (4.1) to (4.6), where $\Lambda^{(1)}$ should be identified with \mathbf{Y}_* . These bounds on \mathbf{Y}_* naturally imply bounds on ϵ_* .

Other bounds on complex ϵ_* have been derived (Milton (1990) - see also Milton (2002), Eqn (22.4)) using the Cherkhev-Gibiansky variational principle (Cherkhev and Gibiansky, 1994). These bounds with $e^{i\theta} = \epsilon_2/|\epsilon_2|$ and ϵ_0 being real and approaching $|\epsilon_2|$, give after dividing them by $|\epsilon_2|$,

$$\begin{aligned} \{\text{Im}[(\epsilon_*/\epsilon_2 - \mathbf{I})^{-1}]\}^{-1} &\geq f_1 \{\text{Im}[(\epsilon_1/\epsilon_2 - 1)^{-1}]\}^{-1} \mathbf{I} + f_2 \{\text{Im}[(1 - \epsilon_0/|\epsilon_2|)^{-1}]\}^{-1} \mathbf{I} \\ &\geq f_1 \{\text{Im}[(\epsilon_1/\epsilon_2 - 1)^{-1}]\}^{-1} \mathbf{I}, \end{aligned} \quad (41)$$

or equivalently

$$\text{Im}[(\epsilon_*/\epsilon_2 - \mathbf{I})^{-1}] \leq \text{Im}[(\epsilon_1/\epsilon_2 - 1)^{-1}] \mathbf{I} / f_1. \quad (42)$$

Similarly, taking $e^{i\theta} = -\epsilon_1/|\epsilon_2|$ and ϵ_0 approaching $-|\epsilon_2|$ we get,

$$\text{Im}[(\epsilon_*/\epsilon_1 - \mathbf{I})^{-1}] \geq \text{Im}[(\epsilon_2/\epsilon_1 - 1)^{-1}] \mathbf{I} / f_2. \quad (43)$$

Now, let us show the equivalence of these bounds with the wedge bounds. Using the relation (36) for \mathbf{Y}_* we get

$$\epsilon_* - \epsilon_2 = f_1(\epsilon_1 - \epsilon_2)[f_2\epsilon_1 - f_1\epsilon_2 + \mathbf{Y}_*]^{-1}[\epsilon_2 + \mathbf{Y}_*] \quad (44)$$

After inverting and multiplying by ϵ_2 we get

$$(\epsilon_*/\epsilon_2 - \mathbf{I})^{-1} = f_1^{-1} f_2 (\mathbf{I} + \mathbf{Y}_*/\epsilon_2)^{-1} + f_1^{-1} (\epsilon_1/\epsilon_2 - 1) \mathbf{I}. \quad (45)$$

Taking the imaginary part of both sides and using (42) we get

$$\text{Im} [1 + \mathbf{Y}_*/\epsilon_2]^{-1} \leq 0, \quad (46)$$

which implies

$$\text{Im} [\mathbf{Y}_*(\epsilon_1, \epsilon_2)/\epsilon_2] \geq 0, \quad (47)$$

which is the wedge bound given by (39). Similarly, the other wedge bound given by (40) follows from (43).

6.B. Optimality of the Wedge Bounds for Two-dimensional Low-loss Composites

Consider a quasistatic two-phase composite with an anisotropic complex effective permittivity tensor denoted by ϵ_* . The constituent phases are assumed to have low loss and the permittivity of phase-1 and phase-2 are denoted by $\epsilon_1 = \epsilon'_1 + \imath\epsilon''_1$ and $\epsilon_2 = \epsilon'_2 + \imath\epsilon''_2$, respectively, where the primes denote the real part and double primes denote the imaginary part. Let f_1 and f_2 denote the volume fractions of phase-1 and phase-2 respectively. The low loss assumption implies that, $\epsilon''_1 \ll \epsilon'_1, \epsilon''_2 \ll \epsilon'_2$.

Without loss of generality (due to homogeneity) we assume the second phase has a constant real-valued dielectric permittivity with zero loss, $\epsilon_2 = \epsilon'_2 > 0$. Since, $\imath\epsilon''_1$ can also be viewed as a small imaginary perturbation to the permittivity $\epsilon_1 = \epsilon'_1 > 0$, we first derive our bounds on the sensitivity when the perturbation is real, and later justify the extension to the case when the perturbation is imaginary (the low loss limit) which as we will show is very straightforward. Hence, the permittivity of the first phase (along with the second phase) is now taken to be real-valued with ϵ''_1 being a small perturbation to the permittivity ϵ_1 , i.e., $\epsilon_1 = \epsilon'_1 + \epsilon''_1$. Our main goal is to now bound the sensitivity $\partial\epsilon_*/\partial\epsilon_1$.

We formulate our problem in two-dimensions as one of finding the coupled bounds on the effective tensors of two properties of a two-phase composite by using the Cherkaev-Gibiansky transformation (Cherkaev and Gibiansky, 1992). Exact coupled bounds for effective tensors of electrical and magnetic properties in a 2d two-phase composite were given by Cherkaev and Gibiansky (1992). We follow the same procedure and use the subsequent results derived therein to find bounds on the sensitivity.

Let $\epsilon_1 = \epsilon'_1 \mathbf{I}$ and $\epsilon_2 = \epsilon'_2 \mathbf{I}$ denote the isotropic unperturbed dielectric permittivity tensors. Now let $\mu_1 = \epsilon'_1 + \epsilon''_1$ denote the perturbed dielectric permittivity of phase-1 for a small real perturbation (ϵ''_1). For simplicity, we define $\mu_2 = \epsilon'_2$ to be the isotropic dielectric permittivity of phase-2 which remains unchanged, i.e., $\mu_2 = \epsilon_2 = \epsilon'_2$.

The effective tensors of the unperturbed and perturbed anisotropic dielectric permittivities are denoted by $\epsilon_*(\epsilon_1, \epsilon_2)$ and $\mu_*(\mu_1, \mu_2)$, respectively. Cherkaev and Gibiansky (1992) gave relations that will be satisfied by all possible pairs of the effective tensors ϵ_* and μ_* . In particular, when the phase properties satisfy the inequality,

$$(\epsilon_1 - \epsilon_2)(\mu_1 - \mu_2) \geq 0, \quad (48)$$

then the effective tensors satisfy the relation,

$$\frac{\epsilon_1}{\mu_1} \mathbf{Y}(\boldsymbol{\mu}_*) \leq \mathbf{Y}(\boldsymbol{\epsilon}_*) \leq \frac{\epsilon_2}{\mu_2} \mathbf{Y}(\boldsymbol{\mu}_*), \quad (49)$$

provided that $\frac{\epsilon_1}{\mu_1} \leq \frac{\epsilon_2}{\mu_2}$. Note that the relation as stated in their original paper

$$\epsilon_1 \mu_1^{-1} \leq \mathbf{Y}(\boldsymbol{\epsilon}_*) \mathbf{Y}(\boldsymbol{\mu}_*)^{-1} \leq \epsilon_2 \mu_2^{-1}, \quad (50)$$

is incorrect, because it assumes that the tensors $\mathbf{Y}(\boldsymbol{\epsilon}_*)$ and $\mathbf{Y}(\boldsymbol{\mu}_*)$ commute which is not true in general. The correct form of the relation is given in (49).

Before proceeding further, we verify that the small perturbations considered here correspond to the case given by the inequality in (48). With $\epsilon_1 = \epsilon'_1$, $\mu_1 = \epsilon'_1 + \epsilon''_1$, and $\mu_2 = \epsilon_2 = \epsilon'_2$ substituted in (48) we have,

$$\begin{aligned} (\epsilon'_1 - \epsilon'_2)(\epsilon'_1 + \epsilon''_1 - \epsilon'_2) &\geq 0, \\ \implies (\epsilon'_1 - \epsilon'_2)^2 + (\epsilon'_1 - \epsilon'_2)\epsilon''_1 &\geq 0. \end{aligned} \quad (51)$$

We can see that for arbitrary small perturbations $\epsilon''_1 \ll \epsilon'_1$, the inequality in (51) holds. Contrast this with the Cherkashev-Gibiansky bounds given in the case when the component phases satisfy the relation $(\epsilon_1 - \epsilon_2)(\mu_1 - \mu_2) \leq 0$. For the problem in this section, this translates to $(\epsilon'_1 - \epsilon'_2)^2 + (\epsilon'_1 - \epsilon'_2)\epsilon''_1 \leq 0$, which does not allow ϵ''_1 to be small, and the corresponding bounds are irrelevant for our purpose.

Since, $\boldsymbol{\mu}_1$ is a small isotropic perturbation of $\boldsymbol{\epsilon}_1$ it is reasonable to assume that the effective Y-tensors also differ by a small perturbation denoted by $\boldsymbol{\delta}$,

$$\mathbf{Y}(\boldsymbol{\epsilon}_*) = \mathbf{Y}(\boldsymbol{\mu}_*) + \boldsymbol{\delta} \quad (52)$$

Using (52) in (49), and noting from our assumption that $\epsilon_2 = \mu_2$, we get,

$$\mathbf{Y}(\boldsymbol{\mu}_*) + \boldsymbol{\delta} \leq \mathbf{Y}(\boldsymbol{\mu}_*). \quad (53)$$

On dividing (53) by ϵ''_1 and further simplifying the result gives,

$$\frac{\boldsymbol{\delta}}{\epsilon''_1} \leq 0, \quad \implies -\frac{\mathbf{Y}(\boldsymbol{\mu}_*) - \mathbf{Y}(\boldsymbol{\epsilon}_*)}{\epsilon''_1} \leq 0 \quad (54)$$

In the limit the perturbations become very small, $\lim \epsilon''_1 \rightarrow 0$, the above inequality gives us bounds on the sensitivity represented by the derivative $\partial \mathbf{Y}(\boldsymbol{\epsilon}_*) / \partial \epsilon_1$:

$$\frac{\partial \mathbf{Y}(\boldsymbol{\epsilon}_*)}{\partial \epsilon_1} \geq 0. \quad (55)$$

Now let the the perturbation ϵ''_1 be purely imaginary (corresponding to low-loss composites). By the

Cauchy-Riemann equations, the sensitivity bound in (55) then implies

$$\text{Im}(\mathbf{Y}_*(\boldsymbol{\epsilon}_*)) = \text{Im}(\boldsymbol{\delta}) \geq 0, \quad (56)$$

which is implied by the wedge bound. For the other bound, we assume $\mu_1 = \epsilon_1$ in the first inequality of (49) and proceed as before. The main outcome here is that the bounds on the sensitivity implied by the Cherkhaev-Gibiansky bounds

$$\frac{\epsilon_1}{\mu_1} \mathbf{Y}(\boldsymbol{\mu}_*) \leq \mathbf{Y}(\boldsymbol{\epsilon}_*) \leq \frac{\epsilon_2}{\mu_2} \mathbf{Y}(\boldsymbol{\mu}_*), \quad (57)$$

are equivalent to the wedge bounds given in (39) and (40) when we take the low-loss limit.

It should be noted that, in addition to (49), when the constituent phases satisfy (48), Cherkhaev and Gibiansky show that the effective tensors also satisfy another condition given by,

$$\frac{\det(\mathbf{Y}(\boldsymbol{\epsilon}_*)/\epsilon_i - \mathbf{R}\mathbf{Y}(\boldsymbol{\mu}_*)^{-1}\mathbf{R}^T\mu_i)}{(1 - \det(\mathbf{Y}(\boldsymbol{\epsilon}_*)/\epsilon_i))(1 - \det^{-1}(\mathbf{Y}(\boldsymbol{\mu}_*)/\mu_i))} \leq \frac{(\epsilon_1\mu_1 - \epsilon_2\mu_2)^2}{(\epsilon_1^2 - \epsilon_2^2)(\mu_2^2 - \mu_1^2)}, \quad i = 1, 2, \quad (58)$$

where

$$\mathbf{R} = \begin{bmatrix} 0 & 1 \\ -1 & 0 \end{bmatrix}. \quad (59)$$

As before, setting $\epsilon_1 = \epsilon'_1$, $\mu_1 = \epsilon'_1 + \epsilon''$, $\mu_2 = \epsilon_2 = \epsilon'_2$ and using the homogeneity of $\mathbf{Y}(\boldsymbol{\epsilon}_*)$ we get

$$\frac{\det(\mathbf{Y}(\boldsymbol{\epsilon}_*/\epsilon_i) - \mathbf{R}\mathbf{Y}(\boldsymbol{\mu}_*/\mu_i)^{-1}\mathbf{R}^T) \det(\mathbf{Y}(\boldsymbol{\mu}_*/\mu_i))}{(1 - \det(\mathbf{Y}(\boldsymbol{\epsilon}_*/\epsilon_i)))(\det(\mathbf{Y}(\boldsymbol{\mu}_*/\mu_i)) - 1)} \leq \frac{(\epsilon'_1(\epsilon'_1 + \epsilon''_1) - \epsilon'^2_2)^2}{(\epsilon'^2_1 - \epsilon'^2_2)(\epsilon'^2_2 - (\epsilon'_1 + \epsilon''_1)^2)}, \quad (60)$$

and using the relation $\det(\mathbf{R}\mathbf{Y}\mathbf{R}^T) = \det(\mathbf{Y})$ gives

$$\frac{\det(\mathbf{Y}(\boldsymbol{\epsilon}_*/\epsilon_i)\mathbf{R}\mathbf{Y}(\boldsymbol{\mu}_*/\mu_i)^{-1}\mathbf{R}^T - \mathbf{I})}{\det(\mathbf{Y}(\boldsymbol{\mu}_*/\mu_i)) + \det(\mathbf{Y}(\boldsymbol{\epsilon}_*/\epsilon_i)) - \det(\mathbf{Y}(\boldsymbol{\epsilon}_*/\epsilon_i))\det(\mathbf{Y}(\boldsymbol{\mu}_*/\mu_i)) - 1} \leq \frac{(\epsilon'_1(\epsilon'_1 + \epsilon''_1) - \epsilon'^2_2)^2}{(\epsilon'^2_1 - \epsilon'^2_2)(\epsilon'^2_2 - (\epsilon'_1 + \epsilon''_1)^2)}. \quad (61)$$

For $i = 1$, the inequality in (61) gives

$$\begin{aligned} & \frac{\det(\mathbf{Y}(\boldsymbol{\epsilon}_*/\epsilon'_1)\mathbf{R}\mathbf{Y}(\boldsymbol{\mu}_*/(\epsilon'_1 + \epsilon''_1))^{-1}\mathbf{R}^T - \mathbf{I})}{\det(\mathbf{Y}(\boldsymbol{\mu}_*/(\epsilon'_1 + \epsilon''_1))) + \det(\mathbf{Y}(\boldsymbol{\epsilon}_*/\epsilon'_1)) - \det(\mathbf{Y}(\boldsymbol{\epsilon}_*/\epsilon'_1))\det(\mathbf{Y}(\boldsymbol{\mu}_*/(\epsilon'_1 + \epsilon''_1))) - 1} \\ & \leq \frac{(\epsilon'_1(\epsilon'_1 + \epsilon''_1) - \epsilon'^2_2)^2}{(\epsilon'^2_1 - \epsilon'^2_2)(\epsilon'^2_2 - (\epsilon'_1 + \epsilon''_1)^2)}, \end{aligned} \quad (62)$$

and for $i = 2$ it gives

$$\frac{\det(\mathbf{Y}(\boldsymbol{\epsilon}_*/\epsilon'_2)\mathbf{R}\mathbf{Y}(\boldsymbol{\mu}_*/\epsilon'_2)^{-1}\mathbf{R}^T - \mathbf{I})}{\det(\mathbf{Y}(\boldsymbol{\mu}_*/\epsilon'_2)) + \det(\mathbf{Y}(\boldsymbol{\epsilon}_*/\epsilon'_2)) - \det(\mathbf{Y}(\boldsymbol{\epsilon}_*/\epsilon'_2))\det(\mathbf{Y}(\boldsymbol{\mu}_*/\epsilon'_2)) - 1} \leq \frac{(\epsilon'_1(\epsilon'_1 + \epsilon''_1) - \epsilon'^2_2)^2}{(\epsilon'^2_1 - \epsilon'^2_2)(\epsilon'^2_2 - (\epsilon'_1 + \epsilon''_1)^2)}. \quad (63)$$

The left hand sides of (62) and (63) approach zero as $\epsilon''_1 \rightarrow 0$, while the right hand sides do not. Therefore,

these inequalities are irrelevant in the small ϵ_1'' limit. Hence, the condition in (58) does not contribute to the sensitivity bounds. As the Cherkaev-Gibiansky bounds are optimal, completely characterizing the G-closure, the associated sensitivity bounds implied by (57) also completely characterize the possible sensitivities for each ϵ_* , and will be attained by the same microgeometries that attain the Cherkaev-Gibiansky bounds. Hence, the wedge bounds should at least almost characterize the possible complex ϵ_* in the low-loss limit.

7. Conclusion

In this work, we systematically investigated the bounds and optimal microstructures associated with the complex uniaxial effective permittivity of two-phase dielectric composites in the quasistatic regime. We demonstrated that the classical bounds on the transverse component ϵ_\perp of the uniaxial effective permittivity, given by Milton (1981a), are not optimal. Through extensive numerical analysis of hierarchical laminates (HLs), we conjecture improved bounds for ϵ_\perp in the form of circular arcs, supported by convex hull computations over millions of generated microstructures. Gaps in attainability of the region Ψ by HLs are perhaps to be expected since the analogous arc to *MCN* (with $\frac{\partial^2 \epsilon_\perp}{\partial \epsilon_1^2} \Big|_{\epsilon_1=1} = -f_1 f_2$) in the isotropic case (with $\frac{\partial^2 \epsilon_*}{\partial \epsilon_1^2} \Big|_{\epsilon_1=1} = -f_1 f_2/3$) also appears to have such gaps (Kern et al., 2020).

We have identified two rank-4 HL families that attain all points on the conjectured bounds. Furthermore, we analyzed the correlation between ϵ_\perp and ϵ_\parallel and developed a design algorithm that allows the construction of HL geometries achieving a specified transverse component ϵ_\perp . We find that the correlated axial components for transverse components on the boundaries AM and AN of the region Ψ are restricted to the boundary of Ω' . Conversely, the correlated transverse components for axial components on the boundary of Ω' lie within the region Ψ as well.

Using the Cherkaev-Gibiansky transformation and the method of translations, we extend the tight bounds developed for isotropic composites by Kern et al. (2020) to the uniaxial case. While the translation-based bounds recover the known isotropic results in the limit $\epsilon_\perp \rightarrow \epsilon_\parallel$, we find that in the uniaxial case when we seek bounds on ϵ_\perp that do not involve ϵ_\parallel (or vice-versa), the specific form of isotropic translation tensor employed does not yield improved bounds over those originally given by Milton (1981a). For anisotropic two-dimensional two-phase composites with low loss, optimal bounds on the sensitivity of the anisotropic effective permittivity with respect to the constituent permittivity ϵ_1 are obtained. The sensitivity bounds imply the optimality of the wedge bounds given by Milton (1987) in the low loss limit.

Several interesting directions remain open for further investigation. First, a rigorous analytical proof of the conjectured optimal bounds on ϵ_\perp remains an open problem. Second, the role of anisotropic translation tensors in deriving tighter theoretical bounds on uniaxial effective permittivity deserves systematic study, extending the work of Kern et al. (2020) to fully anisotropic cases. Third, it would be interesting to see if the conjectured optimal HLs can be replaced by more realistic structures, perhaps using topology optimization. Fourth, given the relevance of uniaxial composites to hyperbolic metamaterials, an important avenue for future work is to apply these design principles to the realization of optimized HMMs with tailored dispersion properties for applications in sub-diffraction imaging, structures for optical negative refraction, spontaneous emission control, and other photonic devices. Finally, it would be good if for two-dimensional, two-phase composites the set of all possible complex effective permittivity tensors could be found and the microgeometries identified

for arbitrary ϵ_1 and ϵ_2 , and not just in the low loss limit.

We hope that the results and methods presented in this work serve as theoretical and computational design tools to guide future explorations in the development of optimized uniaxial composites and advanced hyperbolic metamaterials.

Acknowledgement

The authors are grateful to the National Science Foundation for support through grant DMS-2107926, and to Christian Kern for allowing us to use his results (Figure 4) and for many helpful comments on the manuscript.

References

- Bergman, D. J. 1978. The dielectric constant of a composite material—a problem in classical physics. *Physics Reports* 43(9):377–407.
- Bergman, D. J. 1980a, Jul. Exactly solvable microscopic geometries and rigorous bounds for the complex dielectric constant of a two-component composite material. *Physical Review Letters* 45:148–148.
- Bergman, D. J. 1980b. Exactly solvable microscopic geometries and rigorous bounds for the complex dielectric constant of a two-component composite material. *Physical Review Letters* 44(19):1285.
- Cherkaev, A. V. and L. Gibiansky 1992. The exact coupled bounds for effective tensors of electrical and magnetic properties of two-component two-dimensional composites1. *Proceedings of the Royal Society of Edinburgh Section A: Mathematics* 122(1-2):93–125.
- Cherkaev, A. V. and L. V. Gibiansky 1994. Variational principles for complex conductivity, viscoelasticity, and similar problems in media with complex moduli. *Journal of Mathematical Physics* 35(1):127–145.
- Gibiansky, L. V. and G. W. Milton 1993. On the effective viscoelastic moduli of two-phase media. i. rigorous bounds on the complex bulk modulus. *Proceedings of the Royal Society of London. Series A: Mathematical and Physical Sciences* 440(1908):163–188.
- Hashin, Z. 1962. The elastic moduli of heterogeneous materials. *Journal of Applied Mechanics* 29(1):143–150.
- Hashin, Z. and S. Shtrikman 1962. A variational approach to the theory of the effective magnetic permeability of multiphase materials. *Journal of applied Physics* 33(10):3125–3131.
- Hoffman, A. J., L. Alekseyev, S. S. Howard, K. J. Franz, D. Wasserman, V. A. Podolskiy, E. E. Narimanov, D. L. Sivco, and C. Gmachl 2007. Negative refraction in semiconductor metamaterials. *Nature Materials* 6(12):946–950.
- Jacob, Z., L. V. Alekseyev, and E. Narimanov 2006. Optical hyperlens: far-field imaging beyond the diffraction limit. *Optics Express* 14(18):8247–8256.
- Kern, C., O. D. Miller, and G. W. Milton 2020. Tight bounds on the effective complex permittivity of isotropic composites and related problems. *Physical Review Applied* 14(5):054068.

- Liu, Z., H. Lee, Y. Xiong, C. Sun, and X. Zhang 2007. Far-field optical hyperlens magnifying sub-diffraction-limited objects. *Science* 315(5819):1686–1686.
- Lu, D., J. J. Kan, E. E. Fullerton, and Z. Liu 2014. Enhancing spontaneous emission rates of molecules using nanopatterned multilayer hyperbolic metamaterials. *Nature Nanotechnology* 9(1):48–53.
- Lurie, K. A. and A. V. Cherkhev 1982. Accurate estimates of the conductivity of mixtures formed of two materials in a given proportion (two-dimensional problem). *Doklady Akademii Nauk SSSR* 264:1128–1130. English translation in *Soviet Physics Doklady*, **27**, 461–462 (1982).
- Lurie, K. A. and A. V. Cherkhev 1984. Exact estimates of conductivity of composites formed by two isotropically conducting media taken in prescribed proportion. *Proceedings of the Royal Society of Edinburgh Section A: Mathematics* 99(1-2):71–87.
- Milton, G. W. 1980. Bounds on the complex dielectric constant of a composite material. *Applied Physics Letters* 37(3):300–302.
- Milton, G. W. 1981a. Bounds on the complex permittivity of a two-component composite material. *Journal of Applied Physics* 52(8):5286–5293.
- Milton, G. W. 1981b. Bounds on the transport and optical properties of a two-component composite material. *Journal of Applied Physics* 52(8):5294–5304.
- Milton, G. W. 1987. Multicomponent composites, electrical networks and new types of continued fraction I. *Communications in Mathematical Physics* 111:281–327.
- Milton, G. W. 1990. On characterizing the set of possible effective tensors of composites: the variational method and the translation method. *Communications on Pure and Applied Mathematics* 43(1):63–125.
- Milton, G. W. 2002. The theory of composites. 2002. *Cambridge Monographs on Applied and Computational Mathematics*.
- Murat, F. and L. Tartar 1985. Calcul des variations et homogénéisation. In *Les méthodes de l’homogénéisation: Théorie et Applications en Physique*, pp. 319–369. Paris: Eyrolles.
- Noginov, M., H. Li, Y. A. Barnakov, D. Dryden, G. Nataraj, G. Zhu, C. Bonner, M. Mayy, Z. Jacob, and E. Narimanov 2010. Controlling spontaneous emission with metamaterials. *Optics Letters* 35(11):1863–1865.
- Poddubny, A., I. Iorsh, P. Belov, and Y. Kivshar 2013. Hyperbolic metamaterials. *Nature Photonics* 7(12):948–957.
- Prager, S. 1969. Improved variational bounds on some bulk properties of a two-phase random medium. *The Journal of Chemical Physics* 50(10):4305–4312.
- Salandrino, A. and N. Engheta 2006. Far-field subdiffraction optical microscopy using metamaterial crystals: Theory and simulations. *Physical Review B—Condensed Matter and Materials Physics* 74(7):075103.

- Schulgasser, K. 1977a. Bounds on the conductivity of statistically isotropic polycrystals. *Journal of Physics C: Solid State Physics* 10(3):407.
- Schulgasser, K. 1977b. Concerning the effective transverse conductivity of a two-dimensional two-phase material. *International Journal of Heat and Mass Transfer* 20(12):1273–1280.
- Schulgasser, K. and Z. Hashin 1976. Bounds for effective permittivities of lossy dielectric composites. *Journal of Applied Physics* 47(2):424–427.
- Shekhar, P., J. Atkinson, and Z. Jacob 2014. Hyperbolic metamaterials: fundamentals and applications. *Nano convergence* 1:1–17.
- Smith, D. R., P. Kolinko, and D. Schurig 2004. Negative refraction in indefinite media. *Journal of the Optical Society of America B* 21(5):1032–1043.
- Tartar, L. 1985a. In P. Krée (ed.), *Ennio de Giorgi Colloquium: Papers Presented at a Colloquium Held at the H. Poincaré Institute in November 1983*, p. 168. London: Pitman Publishing Ltd.
- Tartar, L. 1985b. Estimations fines des coefficients homogénéisés. In P. Krée (ed.), *Ennio De Giorgi Colloquium: Papers Presented at a Colloquium held at the H. Poincaré Institute in November 1983*, pp. 168–187. London: Pitman Publishing Ltd. French; English title: *Fine estimations of homogenized coefficients*.
- Tartar, L. 2018. *Estimations of Homogenized Coefficients*, pp. 9–20. Cham: Springer International Publishing. ISBN 978-3-319-97184-1.
- Wiener, O. 1912. Zur theorie der mischkörper für das feld der stationären strömung. *Abhandlungen der Mathematisch-Physikalischen Klasse der Königlich Sächsischen Gesellschaft der Wissenschaften, Leipzig* 32:509–604.
- Yeh, L.-H., I. E. Ivanov, T. Chandler, J. R. Byrum, B. B. Chhun, S.-M. Guo, C. Foltz, E. Hashemi, J. A. Perez-Bermejo, H. Wang, and others 2024. Permittivity tensor imaging: modular label-free imaging of 3d dry mass and 3d orientation at high resolution. *Nature Methods* 21(7):1257–1274.
- Yeh, L.-H., I. E. Ivanov, S.-M. Guo, B. B. Chhun, E. Hashemi, M. H. Han, and S. B. Mehta 2021. upti: uniaxial permittivity tensor imaging of intrinsic density and anisotropy. In *Novel Techniques in Microscopy*, pp. NM3C–4. Optica Publishing Group.